Contents lists available at ScienceDirect

Computers in Biology and Medicine

journal homepage: www.elsevier.com/locate/compbiomed

E2^{UbcH5B}-derived peptide ligands target HECT E3-E2 binding site and block the Ub-dependent SARS-CoV-2 egression: A computational study

Sana Zahid, Mehreen Gul, Shagufta Shafique, Sajid Rashid[*]

National Center for Bioinformatics, Quaid-i-Azam University, Islamabad, 42000, Pakistan

ABSTRACT

Homologous to E6AP carboxyl-terminus (HECT)-type E3 ligase performs ubiquitin (Ub)-proteasomal protein degradation via forming a complex with E2~Ub. Enveloped viruses including SARS-CoV-2 escape from the infected cells by harnessing the E-class vacuolar protein-sorting (ESCRT) machinery and mimic the cellular system through PPAY motif-based linking to HECT Ub ligase activity. In the present study, we have characterized the binding pattern of E2^{UbcH5B} to HECT domains of NEDD4L, WWP1, WWP2, HECW1, and HECW2 through *in silico* analysis to isolate the E2^{UbcH5B}-specific peptide inhibitors that may target SARS-CoV-2 viral egression. Molecular dynamics analysis revealed more opening of E2^{UbcH5B}-binding pocket upon binding to HECT^{NEDD4L}, HECT^{WWP1}, HECT^{WWP2}, HECT^{HECW1}, and HECT^{HECW2}. We observed similar binding pattern for E2^{UbcH5B} and mentioned HECT domains as previously reported for HECT^{NEDD4L} where Trp762, Trp709, and Trp657 residues of HECT^{NEDD4L}, HECT^{WWP1}, and HECT^{WWP2} are involved in making contacts with Ser94 residue of E2^{UbcH5B}. Similarly, corresponding to HECT^{NEDD4L} Tyr756 residue, HECT^{WWP1}, HECT^{WWP2}, HECT^{HECW1}, and HECT^{HECW2}-specific Phe703, Phe651, Phe1387, and Phe1353 residues execute interaction with E2^{UbcH5B}. Our analysis suggests that corresponding to Cys942 of HECT^{NEDD4L}, Cys890, Cys838, Cys1574, and Cys1540 residues of HECT^{WWP1}, HECT^{WWP2}, HECT^{HECW1}, and HECT^{HECW2}, respectively are involved in E2-to-E3 Ub transfer. Furthermore, MM-PBSA free energy calculations revealed favorable energy values for E2^{UbcH5B}-HECT complexes along with the individual residue contributions. Subsequently, two E2^{UbcH5B}-derived peptides (His55-Phe69 and Asn81-Ala96) were tested for their binding abilities against HECT domains of NEDD4L, WWP1, WWP2, HECW1, and HECW2. Their binding was validated through substitution of Phe62, Pro65, Ile84, and Cys85 residues into Ala, which revealed an impaired binding, suggesting that the proposed peptide ligands may selectively target E2-HECT binding and Ub-transfer. Collectively, we propose that peptide-driven blocking of E2-to-HECT Ub loading may limit SARS-CoV-2 egression and spread in the host cells.

1. Introduction

Ubiquitin (Ub) ligases (E3s) regulate the modification sites and the selectivity of target proteins [1–4]. Hence, E3 ligases are the vital specificity factors in Ub signaling and attractive targets for therapeutic applications [5–9]. Homologous to E6AP carboxyl-terminus (HECT) domain Ub ligases (E3s) assist in the Ub transfer to the substrate by forming an Ub thioester intermediate during catalysis [10]. Any dysregulation of HECT-type E3s is closely associated with certain human disorders, including cancer, neurological, and immune disorders [11–13]. The enzyme activity of the HECT-E3 ligases has been linked to the cell egression phase of several RNA viruses through hijacking the endosomal sorting complexes required for the transport machinery

[14–16]. The HECT domain is localized at the C-terminal region of HECT-type E3 ligase and exhibits two structural "lobes" tethered by a flexible linker [13]. The N-terminal "N-lobe" associates with the E2 distal region, while the C-terminal "C-lobe"" contains a HECT catalytic Cys, which receives Ub molecule from the E2 to form a thioester-linked E3~Ub complex.

Approximately 30 HECT E3s in humans act by selectively interacting with distinct E2s and subsequently catalyzing target ubiquitination [3]. HECT-type E3s can be further grouped into several subfamilies based on their distinct N-terminal domains. Among them, NEDD4 (Neuronal precursor cell-expressed developmentally downregulated 4) family is the largest and the best characterized [7,8]. NEDD4 family exhibits 9 members (WWP1/2, NEDD4/NEDD4L, SMURF1/2, HECW1/2, and Itch)

---

with a common N-terminal domain architecture by harboring a C2 domain and 2–4 WW domains that regulate subcellular localization and substrate recognition, respectively [14]. HECT E3 NEDD4 Like E3 Ubiquitin Protein Ligase (NEDD4L) binds and receives Ub from a subset of E2s, including Ub-conjugating Enzymes UbcH5B and Ube2E3 [8].

Recent reports have shown that HECT family members physically associate with certain viral proteins to modulate the release of mature viral particles through the ESCRT (Endosomal Sorting Complex Required for Transport) machinery and regulate endocytosis through ubiquitination [17]. In addition to the lungs of affected patients and COVID-19 mouse models, the mRNA of NEDD4 family members is overexpressed in COVID-19 patients in nasopharyngeal and oropharyngeal swab cells [18]. SARS-CoV-2 is a novel virus with a spherical form and mushroom-shaped proteins on its outer surface known as spikes [19]. SARS-CoV-2 primarily transmits through saliva, droplets, or discharges from an infected person's nose upon coughing or sneezing. Covid-19 has been linked to more than 0.5 billion cases worldwide, with an estimated 6.2 million deaths, and many potential lead molecules are under investigation to combat Covid-19 [20–22]. The N-terminal region of SARS-CoV-2 spike protein contains a PPxY L-domain motif that can hijack the host WW-domain of NEDD4 E3 Ub ligases and, ultimately, the ESCRT complex to enhance virus budding and spread [18]. More importantly, this motif is absent in SARS-CoV, which may explain why SARS-CoV-2 is more contagious than SARS-CoV [23]. Although the COVID-19 pathogenesis is still under investigation, it is evident that innate immunity plays a critical role in the protective or destructive responses to SARS-CoV-2 infection [24]. Thus, HECT family members can influence the outcome and natural history of the COVID-19 infection, as well as non-cell autonomous antiviral defense mechanisms.

The precise mechanism of HECT domain-containing proteins in promoting the SARS-CoV-2 egression and spread via ESCRT machinery is highly ambiguous. The investigations of the dynamic properties of molecular systems are not easily accessible through experimental methods, especially for the larger macromolecular complexes like HECT-E2; therefore, they can only be characterized through computational means. In this study, a wide range of Bioinformatics approaches have been employed to comprehend the comparative binding patterns of E2 and HECT domains of NEDD4L, WWP1, WWP2, HECW1, and HECW2. Furthermore, a detailed MM-PBSA free energy analysis [25–29] has been performed using E2^{UbcH5B}-HECT. Subsequently, we proposed E2-derived peptides that may selectively target HECT and E2 binding site and block viral budding and release via the egress pathway. Overall, the current study may provide a basis for preclinical support and serve as a possible therapeutic option for managing and treating COVID-19.

2. Methodology

2.1. Sequence and structure-based study

Protein sequences of NEDD4L, WWP1, WWP2, HECW1, and HECW2 were retrieved through UniProtKB/Swiss-Prot database (http://www.uniprot.org/). Multiple sequence alignment was performed using FASTA sequences of HECT domains of NEDD4L, WWP1, WWP2, HECW1, and HECW2 through ClustalW tool [30]. BLOSUM substitution matrix with a gap opening penalty (10) and gap extension penalty (0.1) was used. GeneDoc tool was utilized to visualize and manipulate the resulted alignments [31,32]. 3-Dimensional (3D) coordinates of human E2^{UbcH5B} (PDB entry: 2CLW; Resolution: 1.95 Å), E2^{UbcH5B}-NEDD4L (PDB entry: 3JW0; Resolution: 3.10 Å), WWP1 (PDB entry: 5HPS; Resolution: 2.05 Å), and WWP2 (PDB entry: 5TJ8; Resolution: 2.30 Å) were retrieved through Protein data bank [33]. The energy minimization was carried out by UCSF Chimera 1.13.1 [30] using Amber force field.

Comparative modeling is the most accurate computational approach to generate a reliable tertiary protein structure in the case where no known experimentally determined structure exists [34,35]. For this purpose, primary protein sequences for HECW1 and HECW2 were

subjected to BLAST search against PDB database for suitable template(s) search. 3D structures of HECW1 and HECW2 were predicted by MODELLER 9.14 [36] using NEDD4 (PDB ID: 4BBN-A) as a template with sequence identities of 48.94% and 50.13%, respectively (Table S1). MolProbity [37], ProQ [38], ERRAT [39], ProSA-Web [40] and Verify3D [41] tools were utilized to validate the predicted 3D models, followed by model refinements using WinCoot [42]. Afterwards, geometry optimization was carried out using UCSF Chimera 1.13.1. ERRAT estimates structure by calculating non-bonded interactions between carbon, nitrogen and oxygen atoms [39]. The Verify3D server estimates the model quality by comparing 3D-1D profile with good quality known structures. The Z-score calculates model quality by comparing it with the known protein structures [41].

2.2. Molecular docking analysis

Molecular docking analysis of E2^{UbcH5B} against WWP1, WWP2, HECW1, and HECW2 was accomplished using PatchDock server [43]. HECT domains were assigned as receptor molecules and peptides as ligand molecules, whereas other parameters were set as default. PatchDock divides the molecules into concave, convex and flat patches in the form of a Connolly dot surface representation [44]. Subsequently, these complementary patches are compared to generate candidate transformations that are characterized by a scoring function that considers both geometric fit and atomic desolvation energy [45]. Later on, an RMSD clustering is applied to the candidate solutions to discard the redundant solutions. The usage of advanced data structure and spatial pattern detection techniques including geometric hashing and pose clustering yields an optimized binding pose. Furthermore, a refinement and re-scoring tool FireDock was used to check the specificity of the respective interacting protein, which generates a list of ranked models based on their interaction scores, and may distinguish the proper model in first place [46]. E2^{UbcH5B}-NEDD4L (PDB ID: 3JW0) structure was used as a reference for this study. UCSF Chimera 1.13.1 and DIMplot embedded in LigPlus [47] were employed to analyze the residual interactions, such as hydrogen bonding, bond length, hydrophobic and electrostatic interaction.

2.3. Molecular dynamics simulation analysis

In order to gain a deep insight into the mechanism of E2^{UbcH5B} binding to HECT-type E3s, NEDD4L-E2 (PDB ID: 3JW0), WWP1-E2, WWP2-E2, HECW1-E2, and HECW2-E2 complexes were subjected to 150 ns molecular dynamics (MD) simulations. The best docked complexes were simulated to evaluate the stability, folding, conformational changes and dynamic behavior of the interacting proteins. All MD simulations were executed through Groningen Machine for Chemicals Simulation (GROMACS 5.1.4) package [48], installed on a Dell Precision workstation by Amber force field. Briefly, system was solvated by TIP4P water model [49] in a periodic box using a minimum distance of 1 nm, followed by the addition of counter ions (Na$^+$ and Cl$^-$) to neutralize the system. Prior to run MD simulations, initial steric clashes were removed by energy minimization (500 steps) through steepest descent algorithm. System was equilibrated for 1000 ps at 300 K and 1 bar pressure in NVT [50] and NPT [51] ensembles, respectively. Particle Mesh Ewald (PME) algorithm was employed to analyze the long-range electrostatic interactions [52]. Subsequently, PDB files were generated for every 10 ns time interval to investigate the time-dependent behavior and stability of each system. All MD trajectories were analyzed using UCSF Chimera, PyMol (http://www.pymol.org) and GROMACS. GROMACS modules such as *g rmsd, g rmsf, g hbond, g energy, g gyrate,* and *g sasa* were utilized to analyze the stability and behavior of each system [53–55].

2.4. Principal component analysis

To identify the configuration space of inharmonic motion with only a

few degrees of freedom, principal components analysis (PCA) or essential dynamics (ED) were used to reduce the dimensionality of the MD simulations data [56]. PCA is a method for analyzing the MD trajectory and determining the dominant modes in the overall molecular motion. The most important eigenvector projection in Cartesian trajectory coordinates was used to identify the motion of structures in a multidimensional space [57]. In the ED analysis, we created a covariance matrix of backbone Cα-atoms simulation trajectories for apo-E2 and E2-bound HECT proteins by removing rotational and translational movements. Moreover, the eigenvectors and eigenvalues of the covariance matrices, as well as the projections of the first two principal components were computed. The PCA was accomplished using GROMACS built-in utilities such as *gmx_covar* and *gmx_anaeig*.

2.5. Binding free energy calculation

In order to calculate the binding free energy of the system, Poisson-Boltzmann or generalized Born and surface area continuum solvation (MM/PBSA) method [58] was employed. It improves docking energy via incorporating protein flexibility and provides an inclusive energy composition. The equation [1] is used to calculate the binding free energy of ligand-protein complexes:

$$\Delta G_{binding} = G_{complex} - (G_{protein} + G_{ligand}) \qquad [1]$$

$G_{protein}$ and G_{ligand} are the total energies of separated protein and ligand in the solvent, respectively; whereas, $G_{complex}$ is the total free energy of the protein-ligand complex. The free energies for each individual $G_{complex}$, $G_{protein}$ and G_{ligand} were estimated by:

$$G_X = (E_{MM}) + G_{solvation} \qquad [2]$$

Where x is the protein-ligand complex. $G_{solvation}$ is the free energy of solvation and E_{MM} is the molecular mechanics energy. The molecular mechanics potential energy was calculated in vacuum as follows:

$$E_{MM} = E_{bonded} + E_{non\text{-}bonded} = E_{bonded} + (E_{vdw} + E_{elec}) \qquad [3]$$

E_{bonded} is the bonded interaction, including angle, bond, dihedral and improper interactions; whereas, $E_{non\text{-}bonded}$ is the non-bonded interaction that comprises of electrostatic (E_{elec}) and van der Waals (E_{vdw}) interactions. The solvation free energy ($G_{solvation}$) was calculated as the sum of electrostatic solvation free energy (G_{polar}) and apolar solvation free energy ($G_{non\text{-}polar}$):

$$G_{solvation} = G_{polar} + G_{non\text{-}polar} \qquad [4]$$

G_{polar} was estimated using the Poisson-Boltzmann (PB) equation [59] and $G_{non\text{-}polar}$ was computed using a solvent accessible surface area (SASA) as follows:

$$G_{non\text{-}polar} = \gamma SASA + b \qquad [5]$$

Here, γ is a coefficient related to surface tension of the solvent and b is fitting parameter.

2.6. Selection of peptide inhibitors

The coordinates of E2-specific interaction regions (His55-Phe69 and Asn81-Ala96) involved in binding to HECT domains were manually cleaved and saved into a separate file. The energy minimization of these peptides was carried out by UCSF Chimera 1.13.1 using Amber force field. The physicochemical properties of these peptides, including molecular weight, iso-electric point, net charge, average hydrophilicity and ratio of hydrophilic residues/total number of residues were analyzed using Peptide Calculator tool (www.bachem.com/knowledge-center/peptide-calculator/). Peptides may have problems such as truncated side chains that can lead to non-integral net charges. Charge assignment requires explicit hydrogens, which were added by AddH and Add Charge

options of UCSF Chimera version 1.13.1 using the AMBER ff14SB force field. These peptides were re-evaluated for binding to NEDD4L, WWP1, WWP2, HECW1, and HECW2 through PatchDock server [43] and the specificity of the respective interacting protein was checked via Fire-Dock [46].

2.7. Effects of mutation on protein function

In order to select residues for mutational analysis, we recruited six distinct Bioinformatics tools namely, SIFT (Sorting Intolerant From Tolerant) [60,61] (https://sift.jcvi.org/www/SIFT_seq_submit2.html), PANTHER (Protein Analysis Through Evolutionary Relationship) [62] (https://www.pantherdb.org/tools), PolyPhen-2 (Polymorphism Phenotyping v2) [63] (https://genetics.bwh.harvard.edu/pph2/), SNPs&GO [64] (https://snps.biofold.org/snps-and-go/snps-and-go.html), PROVEAN (Protein Variation Effect Analyzer) [65] (https://provean.jcvi.org/index.php), and PredictSNP [66] (https://loschmidt.chemi.muni.cz/predictsnp) to predict the functional effects caused by the mutations induced in the E2 peptide inhibitors. These findings ensured the accuracy and stringency of the results and we considered those mutations as high-risk, which were anticipated as deleterious by all the six programs.

SIFT server uses sequence homology to interpret the effect of amino acid substitution to identify the tolerated and deleterious SNPs. Substitution of amino acid at a particular position with a probability <0.05 is considered as deleterious and intolerant, whereas, probability ≥0.05 is predicted as tolerant [67]. PANTHER program classifies the proteins on the basis of evolutionary relationship, molecular functions and their interactions with other proteins. It analyzes substitution based on position specific evolutionary conservation scores, which is calculated from alignment of various proteins that are evolutionarily related [62]. PolyPhen-2 predicts the functional effect of amino acid substitutions on the protein structure and functions based on sequence-based characterization [63]. I-Mutant 3.0 is based on the Support Vector Machine (SVM) protocol that assesses the change in the protein stability upon point mutation in the form of free energy change (i.e., Gibb's free energy (DDG) values) [68]. SNPs&GO server estimates the human disease related mutations based on the support vector machines (SVM) [64]. PROVEAN is a web server that uses sequence homology to predict the functional effect of an amino acid substitution. The cutoff value of PROVEAN is set at −2.5. Amino acid substitutions that exceed the cut off value were considered as deleterious [65]. PredictSNP tool is a consensus SNP classifier, developed by exploiting six prediction programs (MAPP, PhD-SNP, PolyPhen-1, PolyPhen-2, SIFT and SNAP) to predict the disease related mutations [66]. Additionally, I-Mutant 3.0 [69] and MutPred [70] servers were employed to predict the influence of mutations on the protein stability.

In order to check the reliability of the E2-derived peptide inhibitors, Phe62 and Pro65 residues of peptide inhibitor-1 (His55-Phe69) and Ile84 and Cys85 residues of peptide inhibitor-2 (Asn81-Ala96) were substituted into Alanine via MODELLER 9.14 [36] and redocked them against NEDD4L, WWP1, WWP2, HECW1, and HECW2 via PatchDock server for structural analysis.

3. Results

3.1. Comparative sequence analysis

HECT domains of NEDD4L, WWP1, WWP2, HECW1, and HECW2 share 48–52% sequence similarity with each other, whereas WWP1 and WWP2 exhibit 92.5%, while HECW1 and HECW2 contain 83.5% similarity (Fig. 1A). The sequentially conserved residues among NEDD4L, WWP1, WWP2, HECW1, and HECW2 may help to delineate their structural and functional relationships. In order to elucidate the binding patterns of HECT-type E3s and E2^{UbcH5B}, 3D structures of HECW1 and HECW2 were modeled using NEDD4 coordinates as template (Table S1).
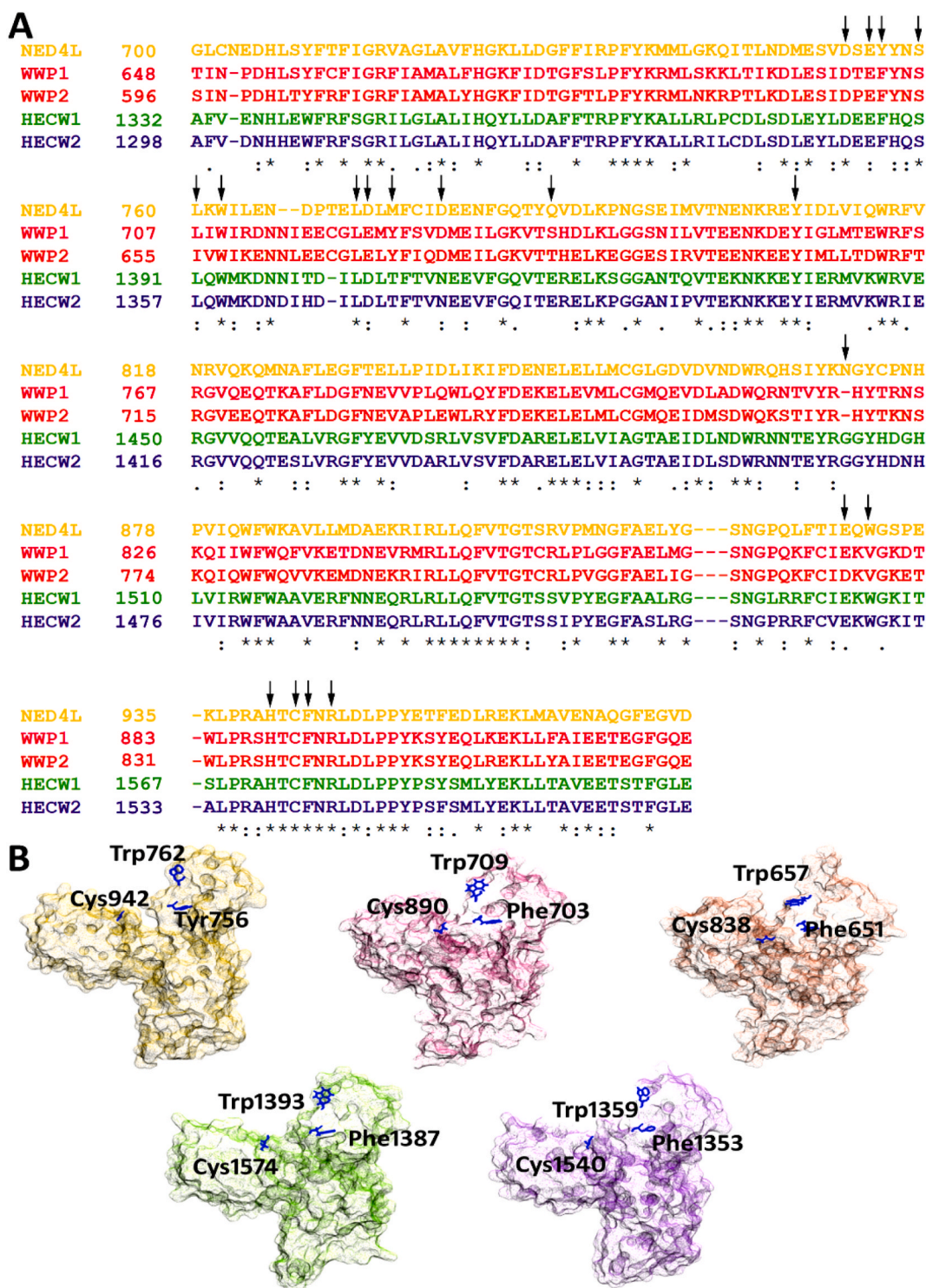
Fig. 1. Multiple sequence alignment analysis for HECT family members. (A) CTD sequence alignment for HECT family members through ClustalW. The arrows depict conserved residues in reference to HECT[NEDD4L] that are involved in E2 binding. The numbering can be referred to UniProtKB. (B) 3D structures of HECT family members that are depicted in surface view along with conserved residues labeled in black color. NEDD4L, WWP1, WWP2, HECW1, and HECW2 are represented in yellow, pink, orange, green, and purple colors, respectively.

The efficacy and reliability of the predicted structures was evaluated by Ramachandran plot, which indicated the existence of 90–95% residues in the favored regions. Subsequent outlier removal and poor rotamer correction refined the predicted models (Table S2). The structures were evaluated through ProSA-web [40]. Verify3D server was utilized to estimate the model(s) quality by comparing it with good quality structures. For all the predicted models, the calculated Z-scores were within

the acceptable range (−3.8 to −7.04). The ERRAT derived values for HECW1 and HECW2 were 85.139 and 80.495, respectively.

The surface views of HECT[NEDD4L], HECT[WWP1], HECT[WWP2], HEC-T[HECW1], and HECT[HECW2] structures depict the conserved residues in the identical regions (Fig. 1B).

Table 1
Interaction analysis for E2^UbcH5B and HECT E3s.

Complex	Hydrogen bonds between E2 and HECT E3s	E2-specific hydrophobic interactions	HECT-specific hydrophobic interactions	Binding Energy (kcal/mol)
E2-NEDD4L	Leu3:Gln787 Lys8:Asp772 Phe62:Ser759 Lys63:Asp753 Lys63:Glu755 Pro118:His940 Leu119:Arg945	Ala2, Lys4, Arg5, Phe31, Thr58, Asp59, Pro64, Asn79, Ser83, Arg90, Pro95, Ala96, Asp116, Pro121	Tyr756, Leu760, Trp762, Leu771, Met774, Asp778, Glu780, Tyr807, Asn871, Glu928, Trp930, Ser942, Phe943	PDB ID: 3JW0
E2-WWP1	Thr58:Glu729 Pro118:Arg819	Met1, Phe31, Pro57, Asp59, Phe62, Lys63, Pro64, Pro65, Lys66, Arg90, Ser91, Gln92, Trp93, Ser94, Pro95, Ala96, Pro121	Asp700, Thr701, Glu702, Asn705, Ser706, Trp709, Gly719, Leu720, Met722, Ser725, Val726, Asp727, Met728, Val734, Arg767, Cys890, Phe891	−22.60
E2-WWP2	Thr58:Asp675 Phe62:Ser654 Lys66:Glu677 Ser91:Ala582 Ser91:Ile647 Ser91:Asp648 Ser91:Glu650	Met1, His55, Phe56, Pro57, Asp59, Lys63, Pro64, Pro65, Val67, Ala68, Asn79, Asn81, Gly82, Ser83, Asp87, Arg90, Gln92, Trp93, Ser94, Pro95, Asp116, Asp117, Pro121	Pro574, Gly583, Lys584, Asn585, Gln590, Ile597, Pro649, Phe651, Trp657, Cys666, Gly667, Leu668, Glu669, Leu670, Ile673, Gln674, Met676, Leu679, Val682, Thr684, Tyr704, Asn816	−22.56
E2-HECW1	Met1:Thr1408 Lys4:Glu1419 Thr58:Glu1412 Lys66:Ser1551 Asn81:Arg1555 Ser83:Arg1555	Ala2, Leu3, Asp29, Phe31, Asp59, Phe62, Lys63, Pro64, Val67, Asn79, Ile84, Cys85, Arg90, Trp93, Pro95, Asp116, Asp117, Pro118, Leu119, Val120, Pro121	Asp1384, Glu1386, Phe1387, Ser1390, Met1394, Leu1403, Leu1405, Thr1406, Val1409, Glu1411, Val1417, Tyr1439, Met1443, Gly1503, Asn1552, Glu1560, Lys1561, Trp1562, Arg1570, Thr1573, Cys1574, Phe1575, Arg1577	−31.56
E2-HECW2	Asp29:Glu1358 His32:Gln1355 Thr53:Ser1356 Thr58:Ser1567 Thr58:Thr1568 Phe62:Arg1536 Lys63:Phe1499 Lys66:Glu1351 Arg72:Leu1369 Arg72:Asp1370 Asn81:Arg1413 Ser83:Glu1352 Arg90:Ser1517 Arg90:Asn1518 Arg90:His1538 Trp93:Arg1536 Met147:Asp1367	Met1, Phe31, Val49, Phe51, Ile54, His55, Asp59, Pro64, Val67, Ala68, Thr70, Thr71, Asp87, Leu89, Ser91, Pro95, Val126, Tyr145 and Ala146	Phe1353, Trp1359, Asp1362, Ile1368, Leu1371, Trp1528, Leu1534, Ala1537, Thr1539, Phe1541, Glu1565, Thr1566, Leu1571	−30.27

3.2. Comparative interaction analysis of E2 with HECT E3s

Through PatchDock analysis, the 10 best docking solutions were designated for the additional enhancement and rescoring scrutiny by FireDock algorithm. For the optimal clusters of E2 and WWP1, WWP2, HECW1, and HECW2 complexes, the statistical scores obtained by PatchDock server were illustrated in Table 1, which depicted a similar binding pattern to that of E2-NEDD4L complex (PDB ID: 3JW0). In all complexes, we observed the involvements of E2-specific Met1, Leu3, Phe31, Thr58, Asp59, Phe62, Lys63, Pro64, Lys66, Asn79, Ser83, Arg90, Pro95, Ala96, Asp116, Pro118, Leu119, and Pro121 residues in HECT E3 binding (Fig. 2). To further characterize the E2 and HECT E3 interaction, we mapped the E2-specific probable regions required for HECT E3 binding.

3.3. Molecular dynamics simulation analysis

To further characterize the stability, folding, conformational adjustments, and dynamic behavior of NEDD4L, WWP1, WWP2, HECW1, and HECW2 upon binding to E2^{UbcH5B}, MD simulation assays were performed. The stability of secondary structure elements, extent of binding mode, and conformational changes of the simulated complexes were assessed by plotting RMSD (Root Mean Square Deviations), RMSF (Root Mean Square Fluctuations), hydrogen bonding, potential energy plots, Rg (Radius of gyration), SASA (Solvent-Accessible Surface Area), and PCA.

3.3.1. Structural stability and flexibility analyses

RMSD for each complex was measured for 150 ns time scale using apo-E2 as a reference. During MD simulation assays, the average Cα RMSD values for NEDD4L-E2, WWP1-E2, WWP2-E2, HECW1-E2, and HECW2-E2 complexes were below 10 Å, suggesting the system stability in all cases (Fig. 3A). Our analysis specified that backbone RMSD profiles for E2^{UbcH5B}-bound WWP2 and HECW1 complexes exhibited a moderate increase in the overall deviation (up to 11 Å), indicating more structural flexibility during binding. However, later on, both systems gained stability at 70 ns, respectively (Fig. 3A).

Subsequent RMSF analysis indicated residual flexibility upon E2^{UbcH5B} binding to HECT E3s (Fig. 3B & C). In E2-bound NEDD4L complex, more prominent fluctuations were observed in Val26-Gly27,
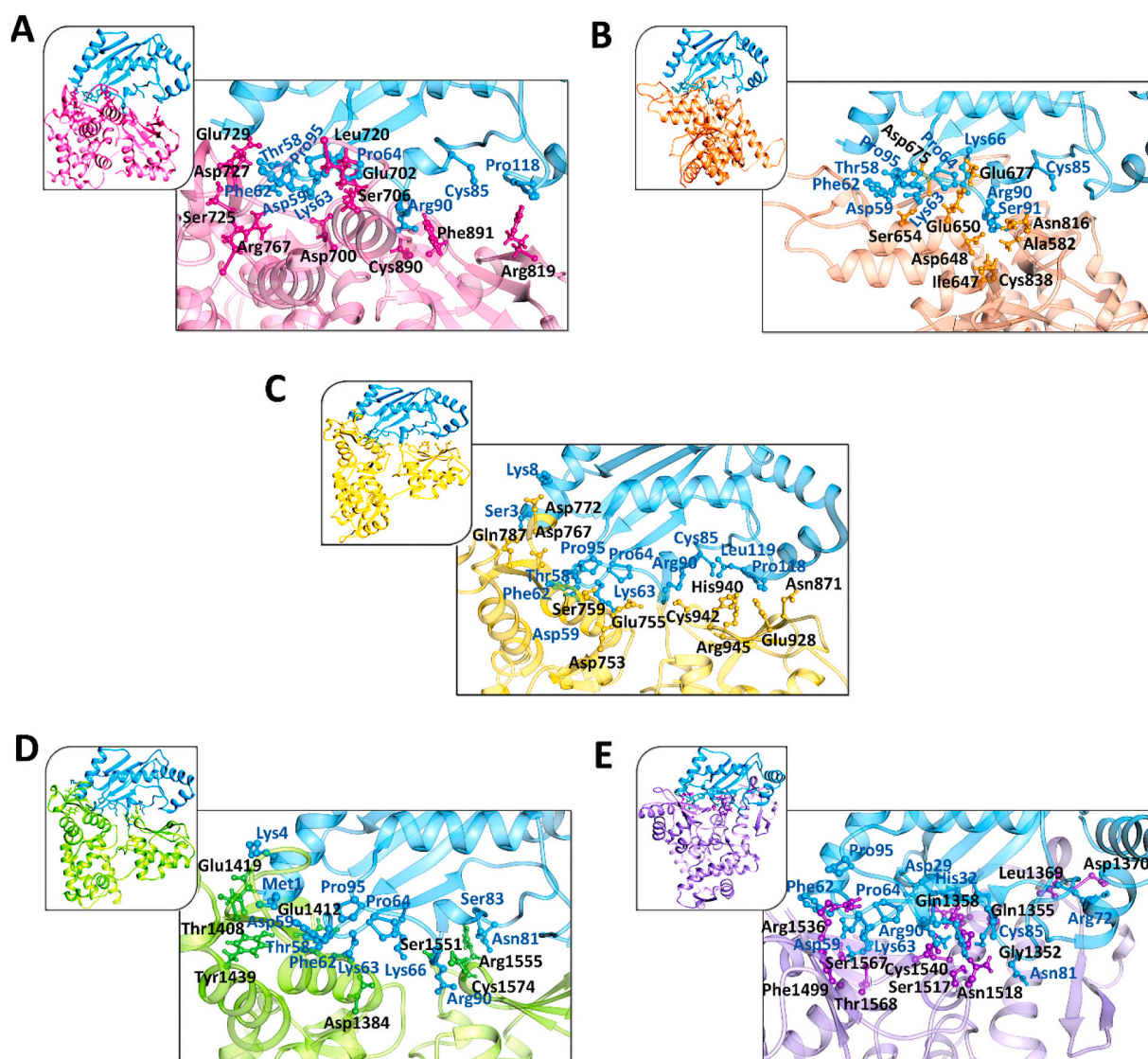

Fig. 2. Binding mode analysis for E2 and HECT domains of NEDD4L, WWP1, WWP2, HECW1, and HECW2. Optimal docked complexes of (A) E2-WWP1, (B) E2-WWP2, (C) E2-NEDD4L, (D) E2-HECW1, and (E) E2-HECW2. E2 is shown in cyan colored ribbon, while the interacting residues are indicated in dark blue sticks. NEDD4L, WWP1, WWP2, HECW1, and HECW2 structures are shown in yellow, pink, orange, green and purple ribbons, respectively, while their respective interacting residues are represented in the ball and stick mode. The interacting residues of E2 and HECTs are labeled in blue and black color, respectively.
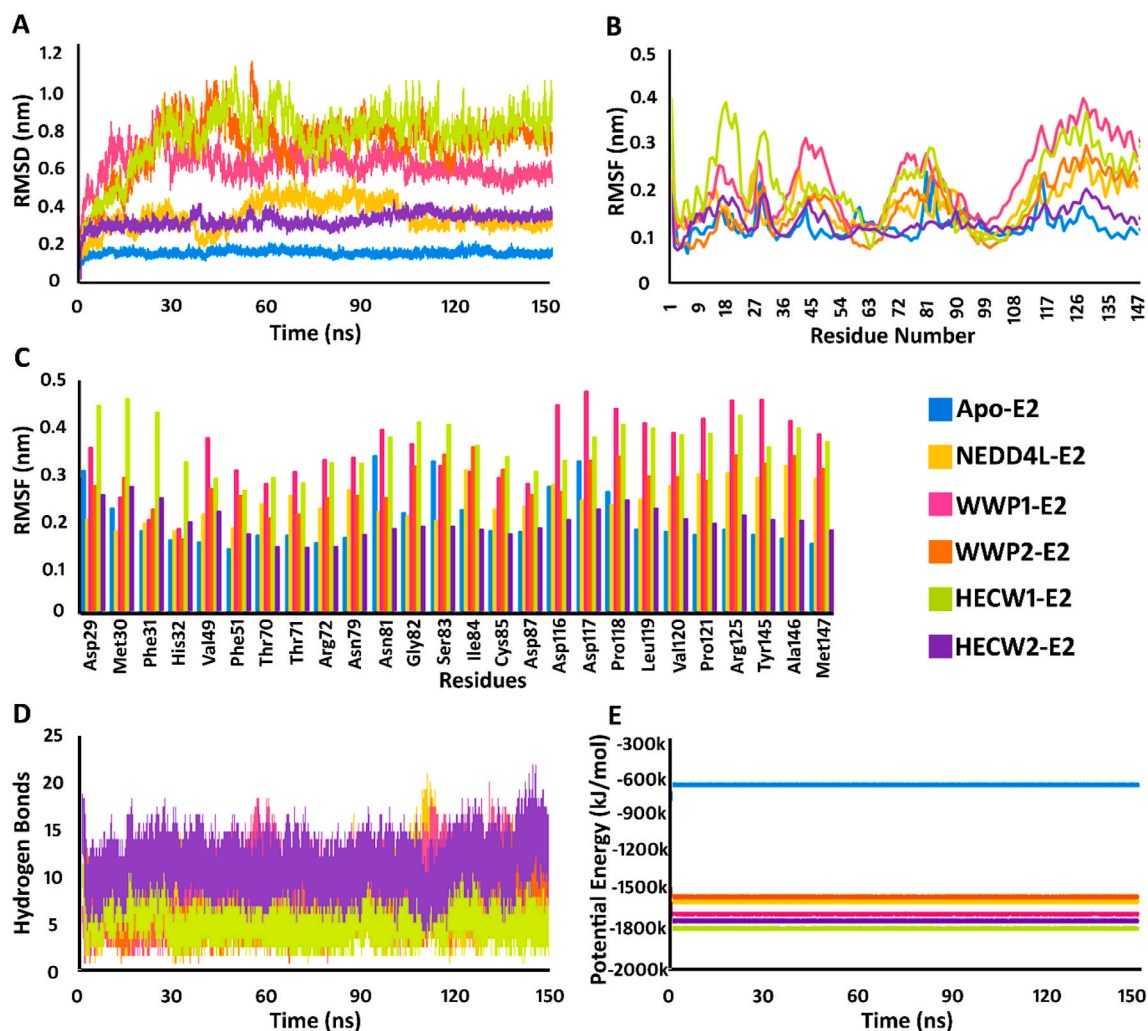
Fig. 3. Plots to investigate the stability, fluctuations, hydrogen bond, and potential energy for apo-E2 and E2-bound NEDD4L, WWP1, WWP2, HECW1 and HECW2. (A) RMSD plotted as a time function. (B) Comparative RMSF plots for apo-E2 and E2-bound forms of NEDD4L, WWP1, WWP2, HECW1 and HECW2. (C) Comparative analysis of the most fluctuating residues is illustrated by bar chart. (D) Intermolecular hydrogen bonding pattern plot. (E) Potential energy plots of E2-HECT complexes. Apo-E2, E2-NEDD4L, E2-WWP1, E2-WWP2, E2-HECW1, and E2-HECW2 are represented in blue, yellow, pink, orange, green, and purple colors, respectively.

Pro40-Asn41, Ile84, Asn114-Pro115, Pro121, and Ala124-Met147 (2.1 Å-2.7 Å) regions, while residues involved in E2-binding remained stable throughout the simulation time. In case of E2-WWP1, major fluctuations (up to 4.0 Å) were observed in Ser43-Gly48, Ile73-Gly82, and Asp117-Tyr145 regions (Fig. 3B and C), while E2 residues involved in binding (Phe31, Pro57-Arg72, and Ser83-Asn114) remained stable during the course of simulation. In case of E2-WWP2, major fluctuations were detected in Asp29-Met30, Ser43- Gly48, Arg72-Leu86, and Asp117-Tyr145 residues (up to 3 Å), while residues involved in E2-binding (His55-Val67, and Ile88-Asn114) were quite stable (Fig. 3B). In E2-HECW1 complex, fluctuations were more common in Glu9-Cys23 (3.8 Å), Asp29-Phe31 (3.2 Å), Pro44-Gly48 (2.1 Å), Tyr74-Ile84 (2.8 Å) and Asp117-Met147 (3.6 Å) regions, located in the immediate vicinity of the binding region (Fig. 3B and C). Correspondingly, in HECW2, Pro17, Gln20, Met30, Pro44, and Pro118-Met147 exhibited higher fluctuation rate (1.2Å-1.5 Å) as compared to other simulated systems, while residues involved in E2-binding were quite stable throughout the simulation time. These results specified that predominant fluctuations occurred in the loop region, while minor fluctuations were observed in the α-domain of E2. The β-domain of E2 remained conserved, which is crucial for the binding stabilization of HECT proteins.

Furthermore, simulated trajectories of E2-bound NEDD4L, WWP1,

WWP2, HECW1, and HECW2 complexes were examined for hydrogen bonding shifts. Inclusively, hydrogen bond interaction pattern remained stable during the entire simulation time (Fig. 3D). More intermolecular hydrogen bonds were observed in E2-bound WWP1 and HECW2 as compared to other simulated systems. Overall, H-bonding pattern implied stable interactions in harmony with the RMSD distribution. The potential energies for apo-E2 and E2-bound NEDD4L, WWP1, WWP2, HECW1, and HECW2 complexes were observed during the course of simulation. The potential energy values were considerably reduced in the E2-bound NEDD4L, WWP1, WWP2, HECW1, and HECW2 complexes as compared to apo-E2. HECW1 depicted the maximum decline in the potential energy as compared to other simulated systems (Fig. 3E).

3.3.2. Structural compactness and SASA analyses

Rg (Radius of gyration) profiles of individual systems were consistent with their corresponding RMSD profiles (Fig. S1A). A higher Rg value implies a lower compactness in the system [71]. Subsequently, E2-bound NEDD4L, WWP1, WWP2, HECW1, and HECW2 exhibited minor compactness than apo-E2. Thus, higher Rg values of complexes than that of apo-E2 suggested firmness in the synergic conformational adaptation owing to E2^{UbcH5B} interaction (Fig. S1A). The surface area of a biomolecule that may be reached by a solvent is known as the

solvent-accessible surface area (SASA). An inferior SASA value denotes a compact protein structure, whereas a higher SASA value implies a diffused structure. Any change in SASA value signifies a modified structural conformation. The SASA values were calculated for apo-E2 versus E2-bound NEDD4L, WWP1, WWP2, HECW1, and HECW2. The average SASA values for apo-E2 were observed in a range of 85–87 nm^2, while E2-bound NEDD4L, WWP1, WWP2, HECW1, and HECW2 systems contained values in the range of 280–290 nm^2. Thus, apo-E2 exhibits lower SASA values than that of E2-bound NEDD4L, WWP1, WWP2, HECW1, and HECW2 (Fig. S1B), which is in accordance with the Rg pattern (Fig. S1A).

3.4. Principal component analysis

PCA or essential dynamics (ED) analysis is widely used to predict the dynamic behavior of a protein. PCA was performed using apo-E2 and its complexes with NEDD4L, WWP1, WWP2, HECW1, and HECW2 to monitor the large-scale collective motions in the trajectories, required for the protein activity. In order to examine the trajectory projections in the phase space, the first two principal components (PC1 and PC2) were selected. Apo-E2 and HECW2-E2 covered a smaller phase space region, while NEDD4L-E2, WWP1-E2, WWP2-E2, and HECW2-E2 occupied a larger phase space region. Conceivably, PCA findings are consistent with the RMSF findings, demonstrating that apo-E2 and HECW2-E2 complex acquired more stability than the rest of E2-bound HECT domain structures (Fig. 4). These analyses suggested that E2-bound NEDD4L, WWP1,

WWP2, HECW1, and HECW2 complexes attained more flexibility as compared to the apo-E2.

3.5. Binding free energy analysis

For free energy landscape analysis, 150 ns simulated trajectories were subjected to MM/PBSA to evaluate the binding contributions of individual residues. E2^{UbcH5B}-NEDD4L, E2^{UbcH5B}–WWP1, E2^{UbcH5B}-WWP2, E2^{UbcH5B}-HECW1, and E2^{UbcH5B}-HECW2 complexes exhibited total binding free energy values of −2496.688, −2439.161, −2326.586, −2042.686, and −2584.382 kJ/mol, respectively (Table 2). The electrostatic (E$_{elec}$), van der Waals (E$_{vdw}$) interactions, and nonpolar solvation (ΔG$_{sol-nonpolar}$) energies negatively contributed, while polar solvation energy (ΔG$_{sol-polar}$) contributed positively to the total binding energy (ΔG$_{binding}$). Our results demonstrated a dominant role of electrostatic interactions in stabilizing the association of E2^{UbcH5B} and HECT proteins. The binding free energy decomposition analysis revealed multiple residual contributions (Fig. 5), which delineated a similar interaction pattern for HECT proteins and E2^{UbcH5B}. Glu684, Val752, Ser754, Leu773, Glu779, Leu790, and Glu802 residues of NEDD4L, Glu632, Asp700, Glu721, Asp727, Glu729, and Asp 738 of WWP1, Glu580, Asp648, Glu665, Glu669, Asp675, and Glu692 of WWP2, Glu1386, Asp1404, Glu1419, and Glu1433 residues of HECW1, and Asp1287, Glu1351, Asp1370, Glu1491, and Glu1557 of HECW2 depicted significant energy contributions during E2 binding (Fig. 5).

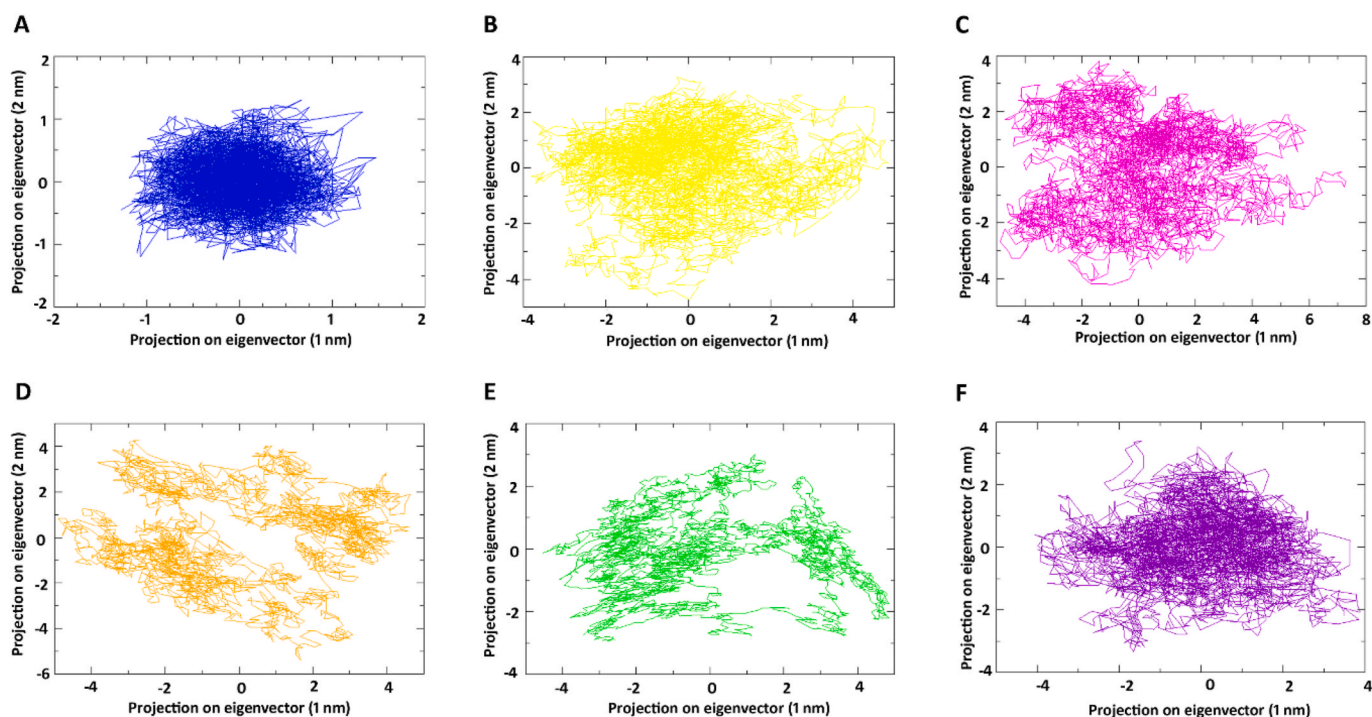In all the cases, the predominant energy contributions of E2^{UbcH5B}

Fig. 4. **2D motion projections for apo-E2 and E2-bound HECT complexes over the first two principal components.** (A) Apo-E2, (B) E2-NEDD4L, (C) E2-WWP1, (D) E2-WWP2, (E) E2-HECW1, and (F) E2-HECW2.

Table 2
Energy contributions (kJ/mol) of E2^{UbcH5B} in complex with NEDD4L, WWP1, WWP2, HECW1, and HECW2.

| Complex	E$_{vdw}$	E$_{elec}$	G$_{sol-polar}$	G$_{sol-non-polar}$	ΔG$_{binding}$
NEDD4L-E2	−390.424±43.284 kJ/mol	−3551.783±256.085 kJ/mol	1495.262±167.467 kJ/mol	−49.743±3.418 kJ/mol	−2496.688±211.449 kJ/mol
WWP1-E2	−385.322±25.729 kJ/mol	−3409.484±191.462 kJ/mol	1402.503±168.263 kJ/mol	−46.858±3.196 kJ/mol	−2439.161±177.897 kJ/mol
WWP2-E2	−476.721±51.863 kJ/mol	−3210.767±347.258 kJ/mol	1416.888±187.026 kJ/mol	−55.986±6.501 kJ/mol	−2326.586±257.206 kJ/mol
HECW1-E2	−349.521±29.311 kJ/mol	−2595.898±213.434 kJ/mol	943.357±139.722 kJ/mol	−40.623±3.674 kJ/mol	−2042.686±187.664 kJ/mol
HECW2-E2	−600.270±28.395 kJ/mol	−3868.102±385.872 kJ/mol	1952.478±206.839 kJ/mol	−68.488±3.175 kJ/mol	−2584.382±246.216 kJ/mol
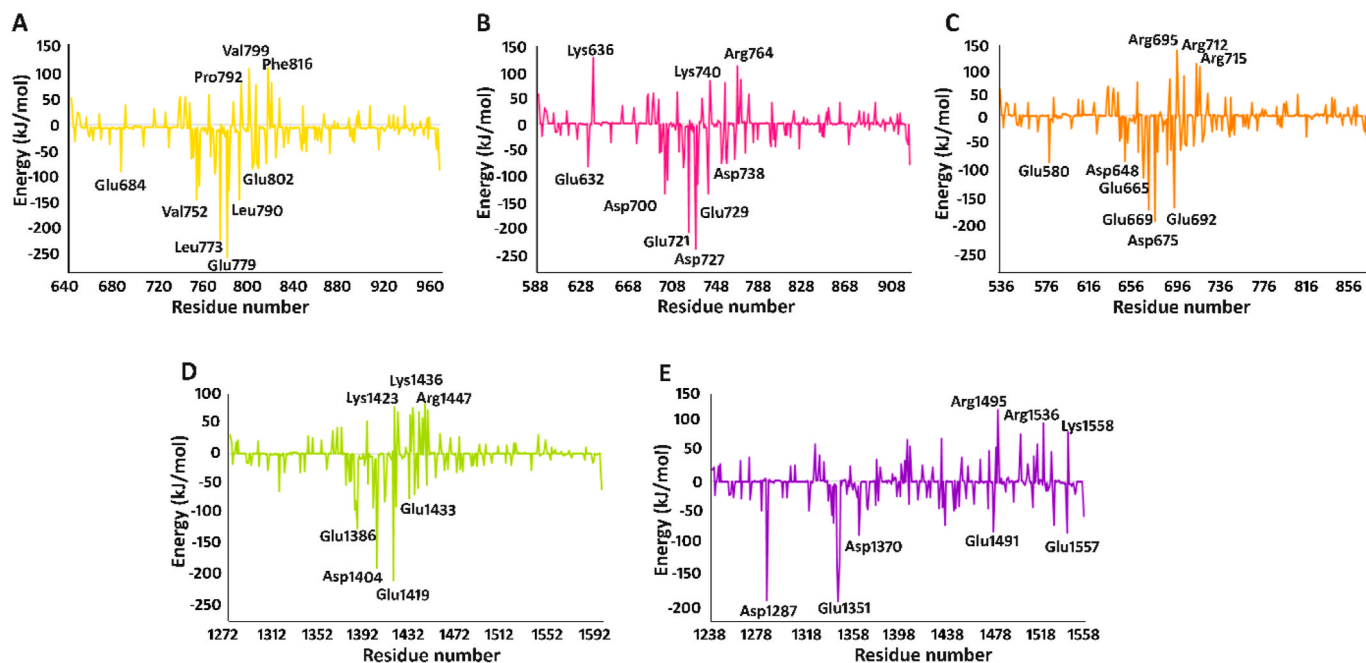
Fig. 5. MM/PBSA analysis of HECT proteins bound to E2^UbcH5B. Binding free energy decomposition at residue basis for (A) NEDD4L, (B) WWP1, (C) WWP2, (D) HECW1, and (E) HECW2 upon binding to E2^UbcH5B.

were due to Lys4, Arg5, Lys8, Arg15, Lys63, Lys66, Arg90, and Lys101 residues (Fig. 6). These data were consistent with the findings of RMSF analysis, as these residues remained stable during the course of simulation run (Fig. 3B and C). The negative binding free energy values for E2^UbcH5B in complex with HECT proteins suggested higher binding affinities (Table 2).

3.6. Conformational transition analysis

To characterize the pronounced conformational switches in comparison to apo-E2 and HECT-bound E2, dynamic trajectories were generated at 30, 60, 90, 120, and 150 ns time scales. Through comparative analysis of NEDD4L, WWP1, WWP2, HECW1, and HECW2-bound E2 with its apo-state, substantial conformational alterations were

witnessed at the vicinity of HECT domain and E2 binding region of HECT domain. Evidently, Cys85, Leu86, Asp87, Arg90, Asn114, Asp116, and Asp117 residues of E2 were involved in the binding pocket formation of E2^UbcH5B, where C-terminal loop region of Ub was well-accommodated into the binding pocket [10]. Prior to MD simulation runs, E2-specific binding pocket was evident in all complexes to accommodate the Ub loop region. During MD simulation, a pocket constriction was observed in the apo-E2 due to an inward pull of E2-specific Asp87 and Asp116 residues. Upon NEDD4L, WWP1, WWP2, HECW1, and HECW2 binding to E2, lateral movements of E2 Asp87 and Asp116 residues facilitated the binding pocket opening. In case of apo-E2, the distance between Asp87 and Asp116 was 8.563 Å, which was increased to 15.933 Å in E2-NEDD4L, 13.721 Å in E2-WWP1, 15.670 Å in E2-WWP2, 12.700 Å in E2-HECW1, and 10.173 Å in E2-HECW2 (Fig. 7). These findings are in
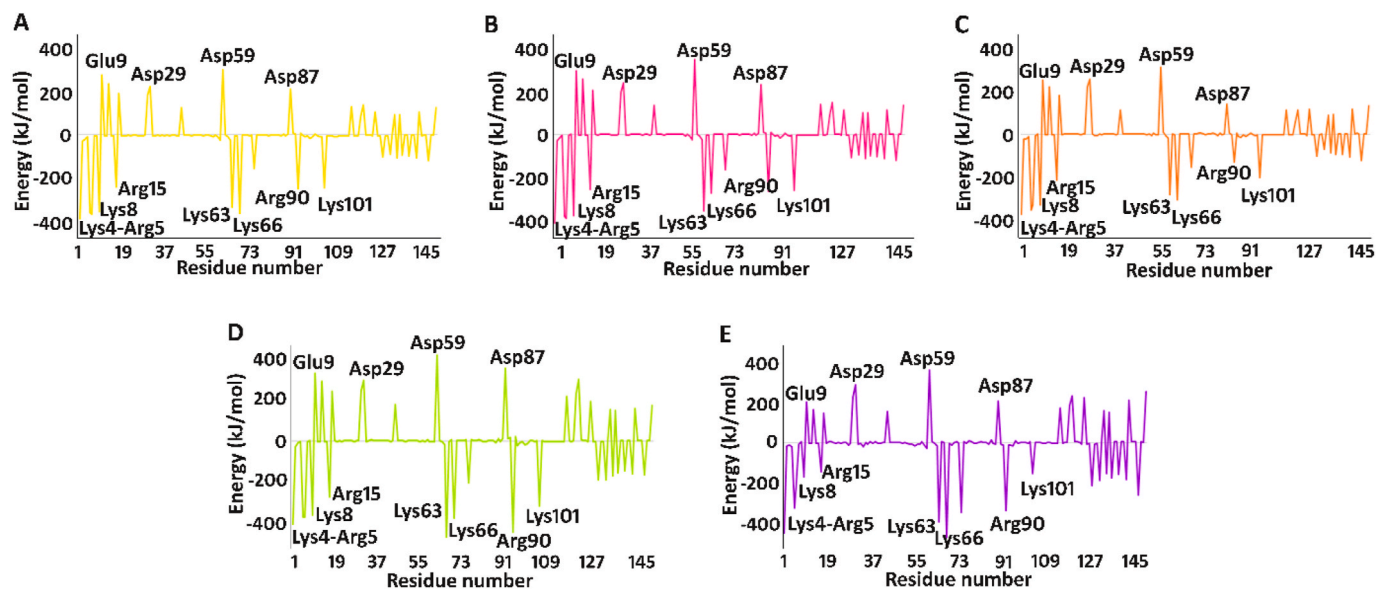

Fig. 6. MM/PBSA analysis of E2^UbcH5B in complex with HECT proteins. Binding free energy decomposition at residue basis for E2^UbcH5B upon binding to (A) NEDD4L, (B) WWP1, (C) WWP2, (D) HECW1, and (E) HECW2.
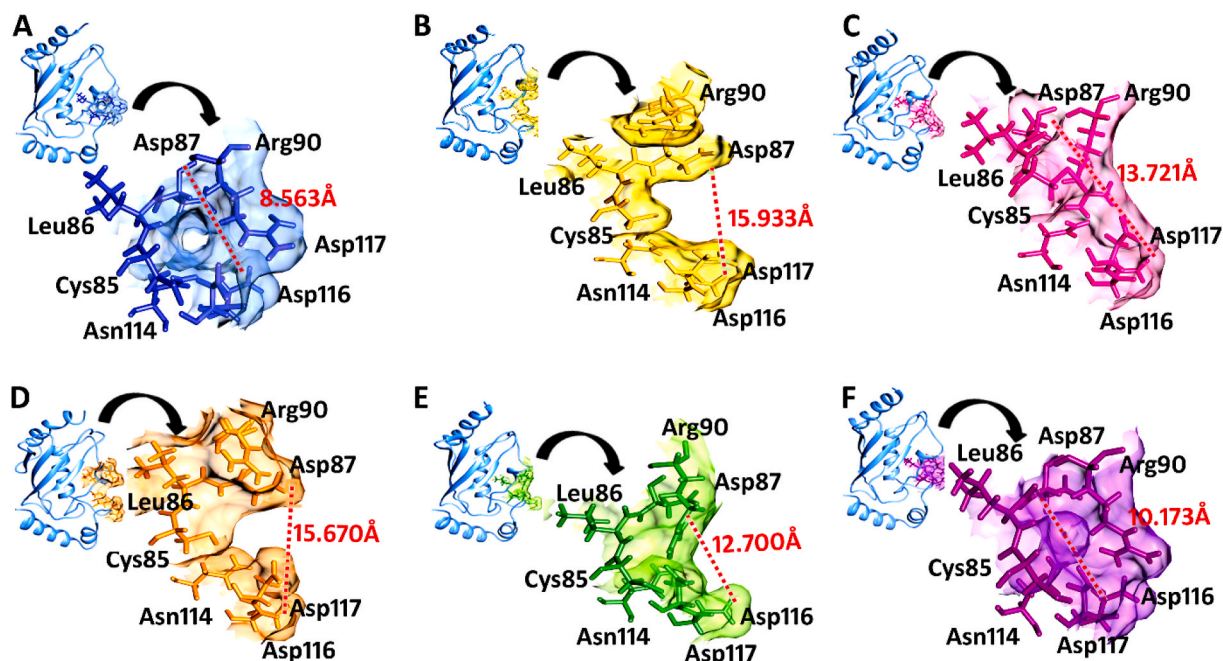
Fig. 7. Binding cavity orientations of apo-E2 and E2-bound WWP1, WWP2, HECW1, and HECW2 proteins. Distances between Asp87 and Asp116 residues of (A) apo-E2 and E2-bound complexes with (B) NEDD4L, (C) WWP1, (D) WWP2, (E) HECW1, and (F) HECW2. NEDD4L, WWP1, WWP2, HECW1, and HECW2 structures are shown in yellow, pink, orange, green and purple ribbons, respectively, while the distance between Asp87 and Asp116 residues is shown by red dotted line.

good agreement to our Rg and PCA results. Higher Rg values for E2^{UbcH5B}-bound NEDD4L, WWP1, WWP2, HECW1, and HECW2 proteins than that of apo-E2 suggested a less tight packing, which led to the opening of E2^{UbcH5B} binding pocket (Fig. S1A).

Generally, Ub binds to Cys85 residue of E2 [10], which is subsequently transferred to the Cys residues of HECT domains (Cys942 of NEDD4L, Cys890 of WWP1, Cys838 of WWP2, Cys1574 of HECW1, and Cys1540 of HECW2). This Cys residue is conserved in all the HECT domains. The conformational transitions occurring in the E2-HECT complexes were deeply analyzed by calculating the distances between E2 and HECT domain Cys, which were 7.892Å, 11.698Å, 12.031Å, 7.125Å, and 8.486Å for NEDD4L, WWP1, WWP2, HECW1, and HECW2, respectively. These distances were increased considerably (Fig. 8) during MD simulation runs (11.810Å, 17.006Å, 16.578Å, 12.705Å, and 13.728Å for NEDD4L, WWP1, WWP2, HECW1, and HECW2, respectively).

Moreover, the apo-E2 and HECT-bound E2 structures were carefully monitored to explore the conformational changes in the E2 structure. Interestingly, a considerable conformational change was perceived in E2 region encompassing Met1-Asp16 residues, resulting in the shortening of α1-helix. Other pronounced conformational changes were observed in the α4-helix of E2, as upon binding, Val120-Ala146 helical region was shortened by splitting into two α-helices. These changes facilitated the movement of E2 towards the binding cavity of HECT domains to assist interaction with NEDD4L, WWP1, WWP2, HECW1, and HECW2. Other than these variations, α-domain remained intact and stable during the entire simulation period.

3.7. Interaction analysis of E2-derived peptides and HECT domains

Next, E2-derived peptides (His55-Phe69 and Asn81-Ala96) were manually cleaved and evaluated for their binding abilities against HECT domains of NEDD4L, WWP1, WWP2, HECW1, and HECW2 through comparative molecular docking analysis. Likewise, E2 binding abilities, these peptides exhibited similar binding patterns against HECT domains of NEDD4L, WWP1, WWP2, HECW1, and HECW2 (Fig. 9).

Subsequently, the physicochemical properties of selected peptides were evaluated (Fig. S2), which revealed the potential importance of E2-peptides in inhibiting Ub transfer to HECT domain by blocking E2-E3 binding. The interaction details and binding energy values for the two peptides and HECT proteins are listed in Table S3. Significant binding contributions of individual residues in full-length E2^{UbcH5B} and HECT domains of NEDD4L, WWP1, WWP2, HECW1, and HECW2 were compared to binding patterns of E2-derived peptide inhibitors (His55-Phe69) and (Asn81-Ala96) to HECT proteins. Highlighted residues in Table S3 are common among the E2-derived peptides and HECT-bound E2. The binding energies of E2-derived peptide inhibitors and HECT proteins were improved considerably, as compared to the binding energies of E2^{UbcH5B} and HECT proteins (Table 1 and Table S3), which indicated more efficient HECT binding abilities of the proposed peptide inhibitors. Thus, our analysis revealed more effective blocking strategy of E2-specific HECT-binding region through the proposed peptide inhibitors.

3.8. Mutational analysis

Amino acid variation in proteins affects the overall protein folding [72,73], stability [74], and functioning [75] leading to various degenerative diseases [76]. Computational approaches are available to analyze the effects of various mutations on the protein structure and function. In order to evaluate the effect of mutations at the E2 and HECT-binding interface, individual residues of E2 peptides were mutated into Alanine and analyzed through various tools. The output generated from the SIFT [60] [61], PANTHER [62], PolyPhen-2 [63], SNPs&GO [64], PROVEAN [65], PredictSNP [66], I-Mutant 3.0 [69], and MutPred [70] tools corroborated the lethal and deleterious effects of four residues, namely Phe62, Pro65, Ile84, and Cys85 of E2 peptides (Table S4).

Based on these finding, we replaced Phe62 and Pro65 residues of peptide-1 and Ile84 and Cys85 of peptide-2 into Alanine and individually docked these peptides against NEDD4L, WWP1, WWP2, HECW1, and HECW2. The binding characteristics and regions of the mutated
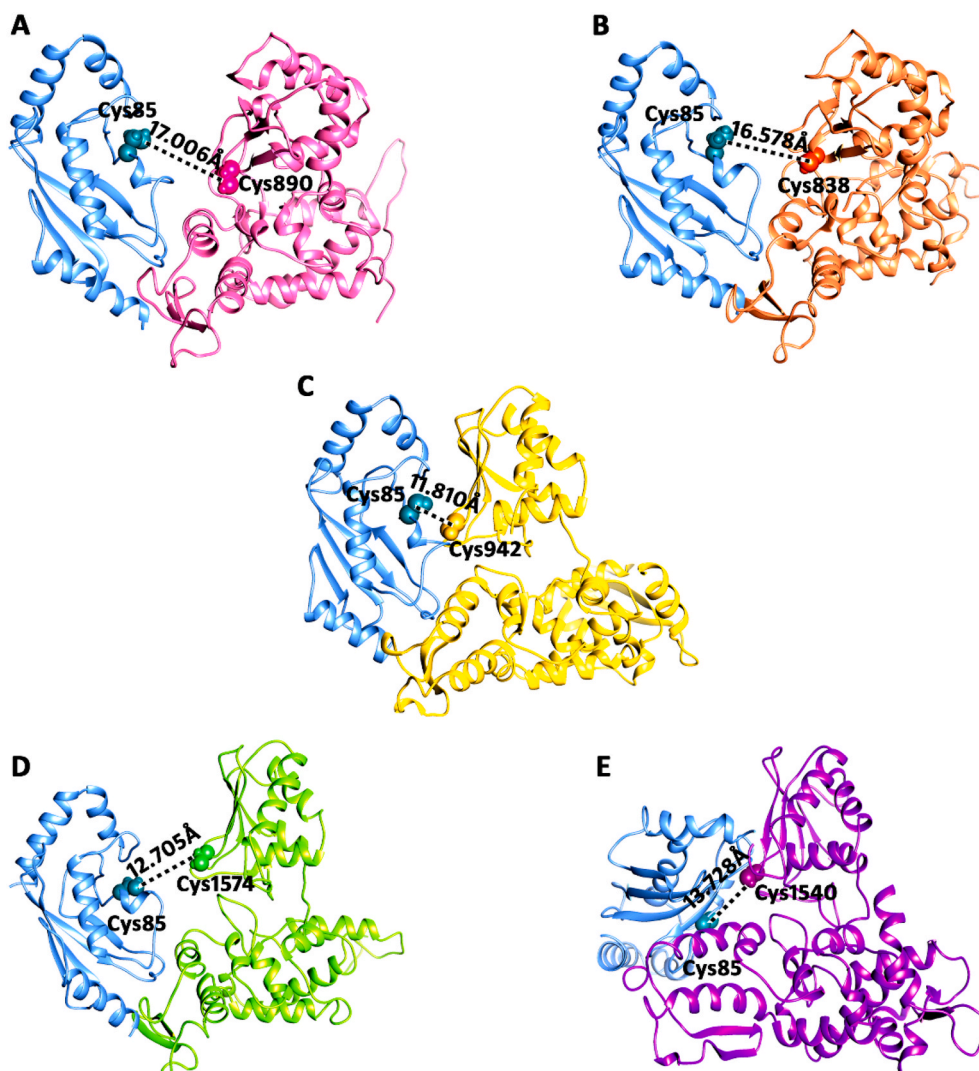
Fig. 8. Comparative distance illustration for cysteine residues of E2-bound WWP1, WWP2, HECW1, and HECW2 with respect to E2-NEDD4L. Distance between Cys85 of E2 and (A) Cys890 of WWP1, (B) Cys838 of WWP2, (C) Cys942 of NEDD4L, (D) Cys1574 of HECW1, and (E) Cys1540 of HECW2.

peptide inhibitors against NEDD4L, WWP1, WWP2, HECW1, and HECW2 were completely altered as compared to the normal E2-derived peptides, confirming the reliability of proposed peptide inhibitors (Table S5; Fig. S3).

4. Discussion

HECT-type E3s promote diverse substrate recognition events in various cellular processes, such as cell cycle progression, oncogenesis, gene transcription, signal transduction, and DNA replication [11,12]. Numerous studies suggest that HECT proteins link viral or cellular proteins (PPxY motif-dependent budding) to the E-class vacuolar protein-sorting pathway (ESCRT) and propagate viral spread via HECT Ub ligase activity [77–79]. HECT proteins (NEDD4L, WWP1, WWP2, HECW1, and HECW2) encompass intrinsic Ub-ligase activities for the substrate binding and ubiquitination through their HECT domains. Recent investigations suggest that during SARS-CoV-2 infection, WWP1, WWP2, and NEDD4L overexpress and colocalize in mice and human lung tissues [18]. Furthermore, NEDD4 and WWP1 physically interact with and ubiquitylate the SARS-CoV-2 S-protein [18]. These findings led us to characterize the E2^{UbcH5B} binding patterns against HECT family members to isolate the E2^{UbcH5B}-specific peptide inhibitors that may abrogate the process of SARS-CoV-2 viral egression by blocking E2-E3 cascade.

During MD simulation runs, notable fluctuations were witnessed in the residues lying at the vicinity of the E2^{UbcH5B} active site due to HECT binding. In contrast, E2 residues involved in HECT binding were quite stable. E2-specific Asp29, Met30, Phe31, His32, Asp116, and Asp117 residues exhibit more fluctuations upon binding to HECW1. Val49, Phe51, Thr70, Thr71, Arg72, Asn79, and Gly82 residues of E2 attain more fluctuations upon binding to NEDD4L, WWP1, WWP2, HECW1, and HECW2 as compared to apo-E2. Similarly, more fluctuations are witnessed in the Cys85, Asp87, Pro118, and Leu119 residues for WWP1, WWP2 and HECW1-bound E2, while RMSF values of these residues in WWP2 and NEDD4L-bound E2 are similar to apo-E2. Val120, Pro121, Arg125, Tyr145, Ala146, and Met147 residues of NEDD4L, WWP1, WWP2 and HECW1-bound E2 exhibit more RMSF values as compared to HECW2-bound E2 and apo-E2. During HECT-E3 interactions, these underlying conformational transitions may promote the positioning of E2 binding cavity and influence the ultimate fate of Ub accommodation and transfer. Probably, different E3s may have varying binding specificities for E2 and Ub contacts that largely rely on the extent of conformational switches and structural rearrangements during the inherent ubiquitination. Evidently, Arg90 acquires an up conformation to Asp87 upon E3 binding, possibly to assist the outward movement of Asp87 and making contact with Ub. The potential role of Asp87 residue has been addressed
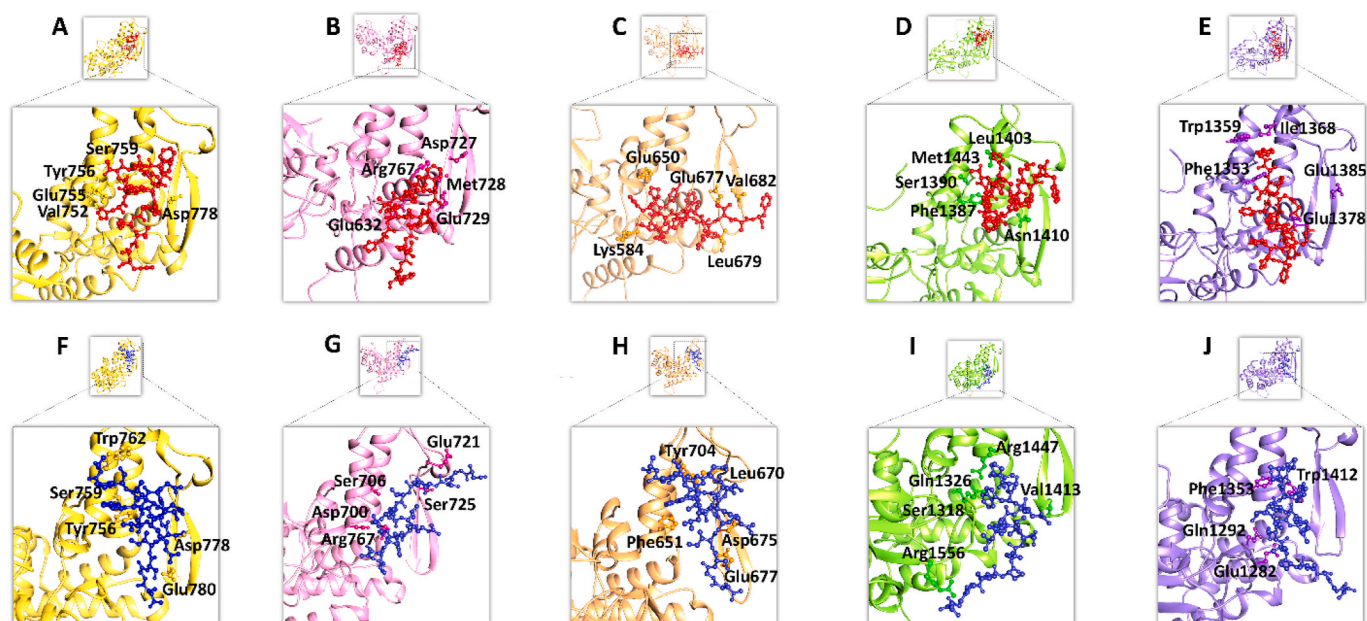
Fig. 9. Binding analysis of E2-derived peptides in complex with NEDD4L, WWP1, WWP2, HECW1 and HECW2. Optimal docked complexes of E2 peptide-1 (His55-Phe69) with (A) NEDD4L, (B) WWP1, (C) WWP2, (D) HECW1 and (E) HECW2. E2 peptide-2 (Asn81-Ala96) in complex with (F) NEDD4L, (G) WWP1, (H) WWP2, (I) HECW1 and (J) HECW2. E2 peptide-1 (His55-Phe69) is shown in red colored atomic structure, while peptide-2 is shown in blue color. NEDD4L, WWP1, WWP2, HECW1, and HECW2 structures are shown in yellow, pink, orange, green, and purple ribbons, respectively, while their respective interacting residues are represented in ball and stick mode and labelled in black color.

in E2:E2~Ub ternary complex as a molecular 'gate' that facilitates the C-terminus of Ub access to the closed E2~Ub complex for Ub transfer [80]. It is unclear how binding cavity orientation differences position the catalytic cysteine and regulate its accessibility during Ub loading. It is interesting to observe the subtle conformational changes contributing in the E2 flexibility induction upon E3 recruitment. The predominant conformational changes were observed in the E2^{UbcH5B} structure including α1-helix shortening and splitting of α4-helix into two helices. These conformational switches promote the E2^{UbcH5B}-binding pocket widening and its stability upon coupling of HECT^{NEDD4L}, HECT^{WWP1}, HECT^{WWP2}, HECT^{HECW1}, and HECT^{HECW2} domains. Based on the prior knowledge of E2^{UbcH5B}-HECT binding [10] [81], our findings delineate exactly similar binding patterns for E2^{UbcH5B} to the C-lobes of HECT-^{NEDD4L}, HECT^{WWP1}, HECT^{WWP2}, HECT^{HECW1}, and HECT^{HECW2}. For example, Trp762, Trp709, and Trp657 residues of HECT^{NEDD4L}, HECT^{WWP1}, and HECT^{WWP2} make contacts with Ser94 residue of E2^{UbcH5B}. The interface linkage of HECT^{NEDD4L} Tyr756 and E2^{UbcH5B} Phe62 [10] is supported by the contributions of HECT^{WWP1}, HECT^{WWP2}, HECT^{HECW1}, and HECT^{HECW2} Phe703, Phe651, Phe1387, and Phe1353 residues, respectively, which share exactly similar side-chain conformations during E2 binding. Similarly, corresponding to the Leu773 position from HECT^{NEDD4L}, E2 interaction is mediated by Met722, Leu670, Leu1405, and Leu1371 residues from HECT^{WWP1}, HECT^{WWP2}, HECT^{HECW1}, and HECT^{HECW2}, respectively. Thus, E2-E3 binding specificity may be induced by subtle sequence variations occurring at the C-lobes of the HECT domains that may preferentially facilitate Ub loading. Generally, the E2-to-HECT Ub loading cascade is initiated by the E1 Ub transfer to E2-Cys85 that is subsequently transferred to the catalytic Cys942 residue of HECT^{NEDD4L} via a thioester-linkage [10]. Our analysis suggests that corresponding to Cys942 residue of HECT^{NEDD4L}, Cys890, Cys838, Cys1574 and Cys1540 residues of HECT^{WWP1}, HECT^{WWP2}, HECT^{HECW1}, and HECT^{HECW2}, respectively may be involved

in E2-to-E3 Ub transfer. Furthermore, E2 and E3 cysteines were separated by 41Å and ~8Å in the crystal structures of UbcH7-HECT^{E6AP} and UbcH5B ~ Ub-HECT^{NEDD4L}, respectively [10]. In our analysis, the predicted distances between E2 and HECT domain catalytic cysteines were 11.8Å, 17.0Å, 16.5Å, 12.7Å, and 13.7Å for NEDD4L, WWP1, WWP2, HECW1, and HECW2, respectively.

To investigate whether the binding of E2^{UbcH5B}-derived peptides targets the HECT binding site, we isolated two peptides (His55-Phe69 and Asn81-Ala96) and docked them against HECT domains of NEDD4L, WWP1, WWP2, HECW1, and HECW2 (Fig. 9; Table S3). Our findings explicate the promising potential of these peptides in hindering the E2 and HECT domain binding, resulting in the inhibition of Ub transfer to the HECT domain. Furthermore, mutational data (swapping of Phe62, Pro65, Ile84, and Cys85 residues into Ala) support that these peptides may selectively target the E2-HECT binding. Consistent with this notion, the exchange of Cys85 into Ala impairs the E2 stability, as Cys85 plays a significant role in Ub binding and transfer [82]. Since E3 HECT domain residues involved in E2 binding are quite conserved, the proposed peptides may effectively bind and target E2-to-E3 Ub-transfer, halting the degradation process of SARS-CoV-2 viral egression. As described earlier [23], the N-terminus of the SARS-CoV-2 S-protein contains a PPAY L-domain motif that has been reported to bind and hijack the host WW-domain of NEDD4 E3 ubiquitin ligases. Due to the absence of the PPxY motif in SARS-CoV, SARS-CoV-2 is more contagious than SARS-CoV. As HECT binding to E2 and Ub facilitates the ubiquitination of SARS-CoV-2 S-protein that hijacks the ESCRT complex to promote egression and spread of COVID-19 (Fig. 10), blocking of HECT domain approach to E2-Ub via proposed peptide inhibitors may restrict viral infection. Due to the sole fact that HECT proteins are overexpressed in concomitance with the SARS-CoV-2 infection, the proposed peptide inhibitors may prove a promising and effective therapeutic strategy.
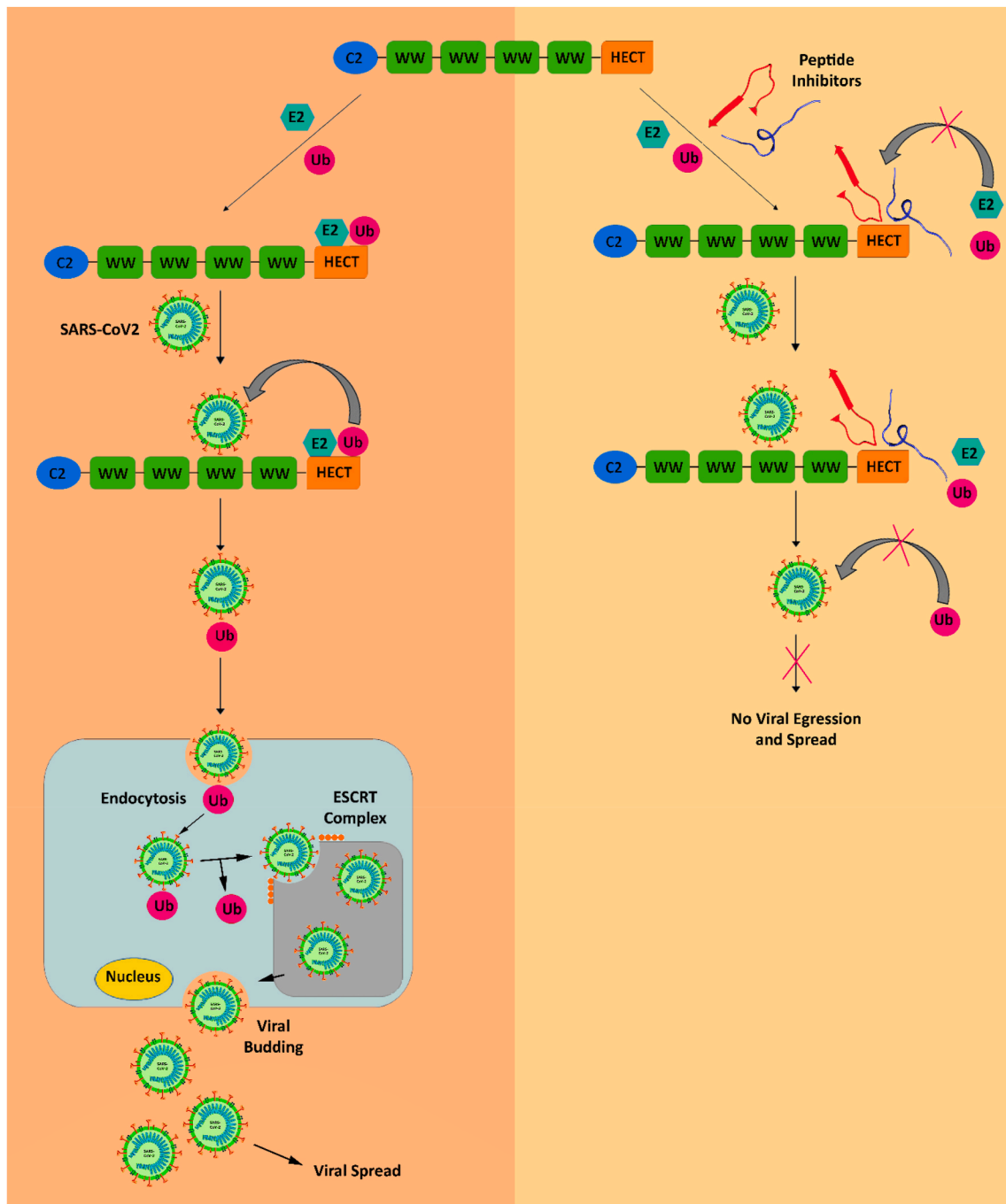
Fig. 10. Schematic illustration of SARS-CoV2 viral egression and spread via ESCRT complex and inhibitory mechanism of SARS-CoV2 cycle via peptide inhibitors. Left side illustrates the normal mechanism of SARS-CoV2 lifecycle. SARS-CoV2 binds to WW domain of HECT proteins via the PPXY motif embedded in its S (Spike)-protein. HECT domain binds to E2 ligase and Ub, transferring its Ub to the S-protein and the ubiquitinated S-protein then enters the cell via endocytosis. It is then recognized by ESCRT complex, which promotes viral budding or egression of the SARS-CoV2 virus causing it to spread violently. On the right side, proposed peptide inhibitors bind to the HECT domain and block the binding site of E2. E2 does not bind to the HECT domain, which in turn, does not transfer Ub to the S-protein, and ultimately, ubiquitination is abrogated. This halts the viral egression and spread of SARS-CoV2 via ESCRT complex.

Author contributions

Conceptualization, Sajid Rashid; Methodology, Sajid Rashid; Formal Analysis, Sana Zahid, Mehreen Gul, Shagufta Shafique; Writing—original draft preparation, Sana Zahid; Writing—review and editing, Sajid Rashid; Supervision, Sajid Rashid. All authors have read and agreed to the published version of the manuscript.

Declaration of competing interest

The authors declare no conflict of interest.

Acknowledgements

Appendix A. Supplementary data

Supplementary data to this article can be found online at https://doi.org/10.1016/j.compbiomed.2022.105660.

References

[1] D. Komander, M. Rape, The ubiquitin code, Annual Review of Biochemistry 81 (2012) 203–229, https://doi.org/10.1146/annurev-biochem-060310-170328.

[2] C.E. Berndsen, C. Wolberger, New insights into ubiquitin E3 ligase mechanism, Nature Structural & Molecular Biology 21 (2014) 301–307, https://doi.org/10.1038/nsmb.2780.

[3] L. Buetow, D.T. Huang, Structural insights into the catalysis and regulation of E3 ubiquitin ligases, Nature Reviews Molecular Cell Biology 17 (2016) 626–642, https://doi.org/10.1038/nrm.2016.91.

[4] N. Zheng, N. Shabek, Ubiquitin ligases: structure, function, and regulation, Annual Review of Biochemistry 86 (2017) 129–157, https://doi.org/10.1146/annurev-biochem-060815-014922.

[5] D. Senft, J. Qi, A.R. Ze'ev, Ubiquitin ligases in oncogenic transformation and cancer therapy, Nature Reviews Cancer 18 (2018) 69–88, https://doi.org/10.1038/nrc.2017.105.

[6] T. Mund, M.J. Lewis, S. Maslen, H.R. Pelham, Peptide and small molecule inhibitors of HECT-type ubiquitin ligases, Proceedings of the National Academy of Sciences 111 (2014) 16736–16741, https://doi.org/10.1073/pnas.1412152111.

[7] V. Fajner, E. Maspero, S. Polo, Targeting HECT-type E3 ligases-insights from catalysis, regulation and inhibitors, FEBS Letters 591 (2017) 2636–2647, https://doi.org/10.1002/1873-3468.12775.

[8] D. Chen, M. Gehringer, S. Lorenz, Developing small-molecule inhibitors of HECT-type ubiquitin ligases for therapeutic applications: challenges and opportunities, ChemBioChem 19 (2018) 2123–2135, https://doi.org/10.1002/cbic.201800321.

[9] S. Zahid, S. Basharat, M. Fakhar, S. Rashid, Molecular dynamics and structural analysis of the binding of COP1 E3 ubiquitin ligase to β-catenin and TRIB pseudokinases, Proteins: Structure, Function, and Bioinformatics 90 (2021) 993–1004, https://doi.org/10.1002/prot.26292.

[10] H.B. Kamadurai, J. Souphron, D.C. Scott, D.M. Duda, D.J. Miller, D. Stringer, R.C. Piper, B.A. Schulman, Insights into ubiquitin transfer cascades from a structure of a UbcH5B~ ubiquitin-HECTNEDD4L complex, Molecular Cell 36 (2009) 1095–1102, https://doi.org/10.1016/j.molcel.2009.11.010.

[11] F. Bernassola, M. Karin, A. Ciechanover, G. Melino, The HECT family of E3 ubiquitin ligases: multiple players in cancer development, Cancer Cell 14 (2008) 10–21, https://doi.org/10.1016/j.ccr.2008.06.001.

[12] D. Wang, L. Ma, B. Wang, J. Liu, W. Wei, E3 ubiquitin ligases in cancer and implications for therapies, Cancer and Metastasis Reviews 36 (2017) 683–702, https://doi.org/10.1007/s10555-017-9703-z.

[13] D. Aki, H. Li, W. Zhang, M. Zheng, C. Elly, J.H. Lee, W. Zou, Y.-C. Liu, The E3 ligases Itch and WWP2 cooperate to limit TH 2 differentiation by enhancing signaling through the TCR, Nature Immunology 19 (2018) 766–775, https://doi.org/10.1038/s41590-018-0137-8.

[14] H. Kawabe, N. Brose, The role of ubiquitylation in nerve cell development, Nature Reviews Neuroscience 12 (2011) 251–268, https://doi.org/10.1038/nrn3009.

[15] J.A. Manning, S. Kumar, Physiological functions of Nedd4-2: lessons from knockout mouse models, Trends in Biochemical Sciences 43 (2018) 635–647, https://doi.org/10.1016/j.tibs.2018.06.004.

[16] C. Debonneville, O. Staub, Participation of the ubiquitin-conjugating enzyme UBE2E3 in Nedd4-2-dependent regulation of the epithelial Na+ channel, Molecular and Cellular Biology 24 (2004) 2397–2409, https://doi.org/10.1128/MCB.24.6.2397-2409.2004.

[17] S.C. Shih, K.E. Sloper-Mould, L. Hicke, Monoubiquitin carries a novel internalization signal that is appended to activated receptors, The EMBO Journal 19 (2000) 187–198, https://doi.org/10.1093/emboj/19.2.187.

[18] G. Novelli, J. Liu, M. Biancolella, T. Alonzi, A. Novelli, J.J. Patten, D. Cocciadiferro, E. Agolini, V.L. Colona, B. Rizzacasa, et al., Inhibition of HECT E3 ligases as potential therapy for COVID-19, Cell Death & Disease 12 (2021) 1–18, https://doi.org/10.1038/s41419-021-03513-1.

[19] N. Vankadari, J.A. Wilce, Emerging COVID-19 coronavirus: glycan shield and structure prediction of spike glycoprotein and its interaction with human CD26, Emerging Microbes & Infections 9 (2020) 601–604, https://doi.org/10.1080/22221751.2020.1739565.

[20] A.A.A.A. Abu-Saleh, I.E. Awad, A. Yadav, R.A. Poirier, Discovery of potent inhibitors for SARS-CoV-2's main protease by ligand-based/structure-based virtual screening, MD simulations, and binding energy calculations, Physical Chemistry Chemical Physics 22 (2020) 23099–23106, https://doi.org/10.1039/D0CP04326E.

[21] A.H. Arshia, S. Shadravan, A. Solhjoo, A. Sakhteman, A. Sami, De novo design of novel protease inhibitor candidates in the treatment of SARS-CoV-2 using deep learning, docking, and molecular dynamic simulations, Computers in Biology and Medicine 139 (2021), 104967, https://doi.org/10.1016/j.compbiomed.2021.104967.

[22] S. Murugesan, S. Kottekad, I. Crasta, S. Sreevathsan, D. Usharani, M.K. Perumal, S.N. Mudliar, Targeting COVID-19 (SARS-CoV-2) main protease through active phytocompounds of ayurvedic medicinal plants-Emblica officinalis (Amla), Phyllanthus niruri Linn.(Bhumi Amla) and Tinospora cordifolia (Giloy)-A molecular docking and simulation study, Computers in Biology and Medicine 136 (2021), 104683, https://doi.org/10.1016/j.compbiomed.2021.104683.

[23] H. Maaroufi, LxxIxE-like motif in spike protein of SARS-CoV-2 that is known to recruit the host PP2A-B56 phosphatase mimics Artepillin C, an immunomodulator, of Brazilian green propolis, BioRxiv (2020), https://doi.org/10.1101/2020.04.01.020941.

[24] L. Petrone, E. Petruccioli, V. Vanini, G. Cuzzi, S.N. Fard, T. Alonzi, C. Castilletti, F. Palmieri, G. Gualano, P. Vittozzi, et al., A whole blood test to measure SARS-CoV-2-specific response in COVID-19 patients, Clinical Microbiology and Infection 27 (2021), 286.e7-286.e13, https://doi.org/10.1016/j.cmi.2020.09.051.

[25] T. Fu, G. Zheng, G. Tu, F. Yang, Y. Chen, X. Yao, X. Li, W. Xue, F. Zhu, Exploring the binding mechanism of metabotropic glutamate receptor 5 negative allosteric modulators in clinical trials by molecular dynamics simulations, ACS Chemical Neuroscience 9 (2018) 1492–1502, https://doi.org/10.1021/acschemneuro.8b00059.

[26] W. Xue, T. Fu, S. Deng, F. Yang, J. Yang, F. Zhu, Molecular mechanism for the allosteric inhibition of the human serotonin transporter by antidepressant escitalopram, ACS Chemical Neuroscience 13 (2022) 340–351, https://doi.org/10.1021/acschemneuro.1c00694.

[27] W. Xue, P. Wang, G. Tu, F. Yang, G. Zheng, X. Li, X. Li, Y. Chen, X. Yao, F. Zhu, Computational identification of the binding mechanism of a triple reuptake inhibitor amitifadine for the treatment of major depressive disorder, Physical Chemistry Chemical Physics 20 (2018) 6606–6616, https://doi.org/10.1039/C7CP07869B.

[28] W. Xue, F. Yang, P. Wang, G. Zheng, Y. Chen, X. Yao, F. Zhu, What contributes to serotonin-norepinephrine reuptake inhibitors' dual-targeting mechanism? The key role of transmembrane domain 6 in human serotonin and norepinephrine transporters revealed by molecular dynamics simulation, ACS Chemical Neuroscience 9 (2018) 1128–1140, https://doi.org/10.1021/acschemneuro.7b00490.

[29] Y. Zhang, J.B. Ying, J.J. Hong, F.C. Li, T.T. Fu, F.Y. Yang, G.X. Zheng, X.J. Yao, Y. Lou, Y. Qiu, et al., How does chirality determine the selective inhibition of histone deacetylase 6? A lesson from trichostatin a enantiomers based on molecular dynamics, ACS Chemical Neuroscience 10 (2019) 2467–2480, https://doi.org/10.1021/acschemneuro.8b00729.

[30] E.C. Meng, E.F. Pettersen, G.S. Couch, C.C. Huang, T.E. Ferrin, Tools for integrated sequence-structure analysis with UCSF Chimera, BMC Bioinformatics 7 (2006) 1–10, https://doi.org/10.1186/1471-2105-7-339.

[31] M.A. Larkin, G. Blackshields, N.P. Brown, R. Chenna, P.A. McGettigan, H. McWilliam, F. Valentin, I.M. Wallace, A. Wilm, R. Lopez, et al., Clustal W and clustal X version 2.0, Bioinformatics 23 (2007) 2947–2948, https://doi.org/10.1093/bioinformatics/btm404.

[32] S. Shafique, N. Bibi, S. Rashid, In silico identification of putative bifunctional Plk1 inhibitors by integrative virtual screening and structural dynamics approach, Journal of Theoretical Biology 388 (2016) 72–84, https://doi.org/10.1016/j.jtbi.2015.10.006.

[33] Y. Shen, A. Bax, Homology modeling of larger proteins guided by chemical shifts, Nature Methods 12 (2015) 747–750, https://doi.org/10.1038/nmeth.3437.

[34] T. Fu, F. Li, Y. Zhang, J. Yin, W. Qiu, X. Li, X. Liu, W. Xin, C. Wang, L. Yu, et al., Varidt 2.0: structural variability of drug transporter, Nucleic Acids Research 50 (2022) D1417–D1431, https://doi.org/10.1093/nar/gkab1013.

[35] H.M. Berman, T.N. Bhat, P.E. Bourne, Z. Feng, G. Gilliland, H. Weissig, J. Westbrook, The Protein Data Bank and the challenge of structural genomics, Nature Structural Biology 7 (2000) 957–959, https://doi.org/10.1093/nar/28.1.235.

[36] B. Webb, A. Sali, Protein structure modeling with MODELLER, Structural Genomics: Methods Mol. Biol. 2199 (2021) 239–255, https://doi.org/10.1007/978-1-0716-0892-0_14.

[37] V.B. Chen, W.B. Arendall, J.J. Headd, D.A. Keedy, R.M. Immormino, G.J. Kapral, L.W. Murray, J.S. Richardson, D.C. Richardson, MolProbity: all-atom structure validation for macromolecular crystallography, Acta Crystallographica Section D: Biological Crystallography 66 (2010) 12–21, https://doi.org/10.1107/S0907444909042073.

[38] B. Wallner, A. Elofsson, Can correct protein models be identified? Protein Science 12 (2003) 1073–1086, https://doi.org/10.1110/ps.0236803.

[39] C. Colovos, T.O. Yeates, Verification of protein structures: patterns of nonbonded atomic interactions, Protein Science 2 (1993) 1511–1519, https://doi.org/10.1002/pro.5560020916.

[40] M. Wiederstein, M.J. Sippl, ProSA-web: interactive web service for the recognition of errors in three-dimensional structures of proteins, Nucleic Acids Research 35 (2007) W407–W410, https://doi.org/10.1093/nar/gkm290.

[41] D. Eisenberg, R. Lüthy, J.U. Bowie, [20] VERIFY3D: assessment of protein models with three-dimensional profiles, Methods in Enzymology 277 (1997) 396–404, https://doi.org/10.1016/S0076-6879(97)77022-8.

[42] P. Emsley, K. Cowtan, Coot: model-building tools for molecular graphics, Acta Crystallographica Section D: Biological Crystallography 60 (2004) 2126–2132, https://doi.org/10.1107/S0907444904019158.

[43] D. Schneidman-Duhovny, Y. Inbar, R. Nussinov, H.J. Wolfson, PatchDock and SymmDock: servers for rigid and symmetric docking, Nucleic Acids Research 33 (2005) W363–W367, https://doi.org/10.1093/nar/gki481.

[44] M.L. Connolly, Analytical molecular surface calculation, Journal of Applied Crystallography 16 (1983) 548–558, https://doi.org/10.1107/S0021889883010985.

[45] N. Andrusier, R. Nussinov, H.J. Wolfson, FireDock: fast interaction refinement in molecular docking, Proteins: Structure, Function, and Bioinformatics 69 (2007) 139–159, https://doi.org/10.1002/prot.21495.

[46] C. Zhang, G. Vasmatzis, J.L. Cornette, C. DeLisi, Determination of atomic desolvation energies from the structures of crystallized proteins, Journal of Molecular Biology 267 (1997) 707–726, https://doi.org/10.1006/jmbi.1996.0859.

[47] A.C. Wallace, R.A. Laskowski, J.M. Thornton, LIGPLOT: a program to generate schematic diagrams of protein-ligand interactions, Protein Engineering, Design and Selection 8 (1995) 127–134, https://doi.org/10.1093/protein/8.2.127.

[48] M.J. Abraham, T. Murtola, R. Schulz, S. Páll, J.C. Smith, B. Hess, E. Lindahl, GROMACS: high performance molecular simulations through multi-level parallelism from laptops to supercomputers, SoftwareX 1 (2015) 19–25, https://doi.org/10.1016/j.softx.2015.06.001.

[49] J. Henriques, M. Skepö, Molecular dynamics simulations of intrinsically disordered proteins: on the accuracy of the TIP4P-D water model and the representativeness of protein disorder models, Journal of chemical theory and computation 12 (2016) 3407–3415, https://doi.org/10.1021/acs.jctc.6b00429.

[50] S. Labík, W.R. Smith, Scaled particle theory and the efficient calculation of the chemical potential of hard spheres in the NVT ensemble, Molecular Simulation 12 (1994) 23–31, https://doi.org/10.1080/08927029408022533.

[51] I.R. McDonald, NpT-ensemble Monte Carlo calculations for binary liquid mixtures, Molecular Physics 23 (1972) 41–58, https://doi.org/10.1080/00268977200100031.

[52] M.J. Abraham, J.E. Gready, Optimization of parameters for molecular dynamics simulation using smooth particle-mesh Ewald in GROMACS 4.5, Journal of Computational Chemistry 32 (2011) 2031–2040, https://doi.org/10.1002/jcc.21773.

[53] W. Kabsch, C. Sander, Dictionary of protein secondary structure: pattern recognition of hydrogen-bonded and geometrical features, Biopolymers: Original Research on Biomolecules 22 (1983) 2577–2637, https://doi.org/10.1002/bip.360221211.

[54] M. Jomhori, H. Mosaddeghi, H. Farzin, Tracking the interaction between single-wall carbon nanotube and SARS-Cov-2 spike glycoprotein: a molecular dynamics simulations study, Computers in Biology and Medicine 136 (2021) 104692, https://doi.org/10.1016/j.compbiomed.2021.104692.

[55] M. Gul, A. Navid, S. Rashid, Structural basis of constitutive c-Src kinase activity due to R175L and W118A mutations, Journal of Biomolecular Structure and Dynamics (2021) 1–12, https://doi.org/10.1080/07391102.2021.2010600.

[56] T. Sindhu, P. Srinivasan, Exploring the binding properties of agonists interacting with human TGR5 using structural modeling, molecular docking and dynamics simulations, RSC Advances 5 (2015) 14202–14213, https://doi.org/10.1039/C4RA16617E.

[57] C.G.P. Doss, B. Rajith, C. Chakraborty, N. NagaSundaram, S.K. Ali, H. Zhu, Structural signature of the G719S-T790M double mutation in the EGFR kinase domain and its response to inhibitors, Scientific Reports 4 (2014) 1–7, https://doi.org/10.1038/srep05868.

[58] R. Kumari, R. Kumar, O.S.D.D. Consortium, A. Lynn, g_mmpbsa A GROMACS tool for high-throughput MM-PBSA calculations, Journal of Chemical Information and Modeling 54 (2014) 1951–1962, https://doi.org/10.1021/ci500020m.

[59] B. Honig, A. Nicholls, Classical electrostatics in biology and chemistry, Science 268 (1995) 1144–1149, https://doi.org/10.1126/science.7761829.

[60] P.C. Ng, S. Henikoff, Predicting the effects of amino acid substitutions on protein function, Annu. Rev. Genomics Hum. Genet. 7 (2006) 61–80, https://doi.org/10.1146/annurev.genom.7.080505.115630.

[61] P. Kumar, S. Henikoff, P.C. Ng, Predicting the effects of coding non-synonymous variants on protein function using the SIFT algorithm, Nature Protocols 4 (2009) 1073–1081, https://doi.org/10.1038/nprot.2009.86.

[62] P.D. Thomas, A. Kejariwal, N. Guo, H. Mi, M.J. Campbell, A. Muruganujan, B. Lazareva-Ulitsky, Applications for protein sequence-function evolution data: mRNA/protein expression analysis and coding SNP scoring tools, Nucleic Acids Research 34 (2006) W645–W650, https://doi.org/10.1093/nar/gkl229.

[63] I.A. Adzhubei, S. Schmidt, L. Peshkin, V.E. Ramensky, A. Gerasimova, P. Bork, A. S. Kondrashov, S.R. Sunyaev, A method and server for predicting damaging missense mutations, Nature Methods 7 (2010) 248–249, https://doi.org/10.1038/nmeth0410-248.

[64] E. Capriotti, R. Calabrese, P. Fariselli, P.L. Martelli, R.B. Altman, R. Casadio, WS-SNPs&GO: a web server for predicting the deleterious effect of human protein variants using functional annotation, BMC Genomics 14 (2013) 1–7, https://doi.org/10.1186/1471-2164-14-S3-S6.

[65] Y. Choi, A.P. Chan, PROVEAN web server: a tool to predict the functional effect of amino acid substitutions and indels, Bioinformatics 31 (2015) 2745–2747, https://doi.org/10.1093/bioinformatics/btv195.

[66] J. Bendl, J. Stourac, O. Salanda, A. Pavelka, E.D. Wieben, J. Zendulka, J. Brezovsky, J. Damborsky, PredictSNP: robust and accurate consensus classifier for prediction of disease-related mutations, PLoS Computational Biology 10 (2014), e1003440, https://doi.org/10.1371/journal.pcbi.1003440.

[67] A. Khokhlatchev, S. Rabizadeh, R. Xavier, M. Nedwidek, T. Chen, X. Zhang, B. Seed, J. Avruch, Identification of a novel Ras-regulated proapoptotic pathway, Current Biology 12 (2002) 253–265, https://doi.org/10.1016/S0960-9822(02)00683-8.

[68] F.I. Khan, M. Shahbaaz, K. Bisetty, A. Waheed, W.S. Sly, F. Ahmad, M.I. Hassan, Large scale analysis of the mutational landscape in β-glucuronidase: a major player of mucopolysaccharidosis type VII, Gene 576 (2016) 36–44, https://doi.org/10.1016/j.gene.2015.09.062.

[69] E. Capriotti, P. Fariselli, R. Casadio, I-Mutant 2. 0: predicting stability changes upon mutation from the protein sequence or structure, Nucleic Acids Research 33 (2005) W306–W310, https://doi.org/10.1093/nar/gki375.

[70] V. Pejaver, J. Urresti, J. Lugo-Martinez, K.A. Pagel, G.N. Lin, H.-J. Nam, M. Mort, D.N. Cooper, J. Sebat, L.M. Iakoucheva, et al., MutPred2: inferring the molecular and phenotypic impact of amino acid variants, Nature communications 11 (2020) 1–13, https://doi.org/10.1038/s41467-020-19669-x.

[71] S. Shafique, S. Rashid, Structural basis of βTrCP1-associated GLI3 processing, Scientific Reports 9 (2019) 1–13, https://doi.org/10.1038/s41598-019-43392-3.

[72] M. Alfalah, M. Keiser, T. Leeb, K.P. Zimmer, H.Y. Naim, Compound heterozygous mutations affect protein folding and function in patients with congenital sucrase-isomaltase deficiency, Gastroenterology 136 (2009) 883–892, https://doi.org/10.1053/j.gastro.2008.11.038.

[73] M. Lorch, J.M. Mason, R.B. Sessions, A.R. Clarke, Effects of mutations on the thermodynamics of a protein folding reaction: implications for the mechanism of formation of the intermediate and transition states, Biochemistry 39 (2000) 3480–3485, https://doi.org/10.1021/bi9923510.

[74] C.G.P. Doss, B. Rajith, N. Garwasis, P.R. Mathew, A.S. Raju, K. Apoorva, D. William, N.R. Sadhana, T. Himani, I.P. Dike, Screening of mutations affecting protein stability and dynamics of FGFR1—a simulation analysis, Applied & Translational Genomics 1 (2012) 37–43, https://doi.org/10.1016/j.atg.2012.06.002.

[75] S. Yamada, Y. Suzuki, T. Suzuki, M.Q. Le, C.A. Nidom, Y. Sakai-Tagawa, Y. Muramoto, M. Ito, M. Kiso, T. Horimoto, et al., Haemagglutinin mutations responsible for the binding of H5N1 influenza A viruses to human-type receptors, Nature 444 (2006) 378–382, https://doi.org/10.1038/nature05264.

[76] D. Blocquel, L. Sun, Z. Matuszek, S. Li, T. Weber, B. Kuhle, G. Kooi, N. Wei, J. Baets, T. Pan, et al., CMT disease severity correlates with mutation-induced open conformation of histidyl-tRNA synthetase, not aminoacylation loss, in patient cells, Proceedings of the National Academy of Sciences 116 (2019) 19440–19448, https://doi.org/10.1073/pnas.1908288116.

[77] C. Fukumoto, D. Nakashima, A. Kasamatsu, T. Unozawa, M. Shida-Sakazume, M. Higo, K. Ogawara, H. Yokoe, M. Shiiba, H. Tanzawa, et al., WWP2 is overexpressed in human oral cancer, determining tumor size and poor prognosis in patients: downregulation of WWP2 inhibits the AKT signaling and tumor growth in mice, Oncoscience 1 (2014) 807, https://doi.org/10.18632/oncoscience.101.

[78] A.E. Clements, V. Bravo, C. Koivisto, D.E. Cohn, G. Leone, WWP2 and its association with PTEN in endometrial cancer, Gynecologic Oncology Reports 13 (2015) 26–29, https://doi.org/10.1016/j.gore.2015.05.004.

[79] S.M. Soond, P.G. Smith, L. Wahl, T.E. Swingler, I.M. Clark, A.M. Hemmings, A. Chantry, Novel WWP2 ubiquitin ligase isoforms as potential prognostic markers and molecular targets in cancer, Biochimica et Biophysica Acta (BBA)-Molecular Basis of Disease 1832 (2013) 2127–2135, https://doi.org/10.1016/j.bbadis.2013.08.001.

[80] M.B. Metzger, J.N. Pruneda, R.E. Klevit, A.M. Weissman, RING-type E3 ligases: master manipulators of E2 ubiquitin-conjugating enzymes and ubiquitination, Biochimica et Biophysica Acta (BBA)-Molecular Cell Research 1843 (2014) 47–60, https://doi.org/10.1016/j.bbamcr.2013.05.026.

[81] U. Nuber, M. Scheffner, Identification of determinants in E2 ubiquitin-conjugating enzymes required for hect E3 ubiquitin-protein ligase interaction, Journal of Biological Chemistry 274 (1999) 7576–7582, https://doi.org/10.1074/jbc.274.11.7576.

[82] H. Gonen, B. Bercovich, A. Orian, A. Carrano, C. Takizawa, K. Yamanaka, M. Pagano, K. Iwai, A. Ciechanover, Identification of the ubiquitin carrier proteins, E2s, involved in signal-induced conjugation and subsequent degradation of IκBα, Journal of Biological Chemistry 274 (1999) 14823–14830, https://doi.org/10.1074/jbc.274.21.14823.